Interplay between dressed and strong-axial-field states in nitrogen vacancy centers for quantum sensing and computation

Original
Interplay between dressed and strong-axial-field states in nitrogen vacancy centers for quantum sensing and computation / Zanelli, G.; Moreva, E.; Bernardi, E.; Losero, E.; Ditalia Tchernij, S.; Forneris, J.; Pastuović, Ž.; Traina, P.; Degiovanni, I. P.; Genovese, M.. - In: PHYSICAL REVIEW. B. - ISSN 2469-9950. - 112:23(2025), pp. 235201-235211. [10.1103/3mlm-jjqq]

Publisher:
American Physical Society

Published
DOI:10.1103/3mlm-jjqq

PHYSICAL REVIEW B **112**, 235201 (2025)

Interplay between dressed and strong-axial-field states in nitrogen vacancy centers for quantum sensing and computation

G. Zanelli,[1,2] E. Moreva,[1] E. Bernardi,[1,*] E. Losero,[1] S. Ditalia Tchernij,[2,3] J. Forneris,[2,3]
Ž. Pastuović,[4] P. Traina,[1] I. P. Degiovanni,[1] and M. Genovese[1,3]
[1]*Istituto Nazionale di Ricerca Metrologica (INRiM), Strada delle cacce 91, Torino, Italy*
[2]*Physics Department and NIS Centre of Excellence - University of Torino, Torino, Italy*
[3]*Istituto Nazionale di Fisica Nucleare (INFN) Sez. Torino, Torino, Italy*
[4]*Centre for Accelerator Science, Australian Nuclear Science and Technology Organisation,*
New Illawarra rd., Lucas Heights, New South Wales 2234, Australia

(Received 21 February 2025; accepted 3 November 2025; published 8 December 2025)

The nitrogen vacancy (NV) center in diamond is an intriguing electronic spin system with applications in quantum radiometry, sensing, and computation. In those experiments, a bias magnetic field is commonly applied along the NV symmetry axis to eliminate the triplet ground-state manifold's degeneracy ($S = 1$). In this configuration, the eigenvectors of the NV spin's projection along its axis are called strong-axial-field states. Conversely, in some experiments, a weak magnetic field is applied orthogonally to the NV symmetry axis, leading to eigenstates that are balanced linear superpositions of strong-axial-field states, referred to as dressed states. The latter are sensitive to environmental magnetic noise at the second order, allowing to perform magnetic field protected measurements while providing increased coherence times. However, if a small axial magnetic field is added in this regime, the linear superposition of strong-axial-field states becomes unbalanced. This paper presents a comprehensive study of free induction decay (FID) measurements performed on an NV center ensemble in the presence of strain and weak orthogonal magnetic field, as a function of a small magnetic field applied along the NV symmetry axis. The simultaneous detection of dressed states and unbalanced superpositions of strong-axial-field states in a single FID measurement is shown, gaining insight into coherence time, nuclear spin, and the interplay between temperature and magnetic field sensitivity. The discussion concludes by describing how the simultaneous presence of magnetically sensitive and insensitive states opens up appealing possibilities for both sensing and quantum computation applications.

DOI: 10.1103/3mlm-jjqq

I. INTRODUCTION

The use of quantum states to sense physical observables, known as quantum sensing [1,2], has demonstrated to be of factual advancement in a plethora of diverse applications (spanning from magnetometry, gravitational wave detection, and quantum thermodynamics) [3–12]. However, isolating a sensor from different sources of noise represents a major challenge in high-precision quantum sensing. Among several classes of quantum sensors, the nitrogen vacancy (NV) center in diamond has been extensively studied as a high-sensitivity nanoscale sensor. More precisely, the NV is an optically active point defect composed of a single substitutional nitrogen and a lattice vacancy in nearest-neighbor configuration; this structure leads to an electronic spin triplet configuration $S = 1$, which can be exploited via spin resonance techniques, allowing for the so-called optically detected magnetic resonance (ODMR) [13] (for an introductory description of NV levels structure and ODMR principle see [14]). NV-based sensing is commonly carried out by monitoring the effect of environmental variables on the dynamics of the NV center; this scheme is enabled by three main features [15]: (i) the spin state can be controlled using microwave radiation; (ii) the initialization and readout can be performed optically; (iii) the system presents coherence times T_2^* in the order of tens of microseconds at room temperature [14,16].

Various techniques have been introduced to make measurements selective on single physical observables, i.e., temperature or magnetic field. For example, thermal echo [17], D-Ramsey pulse sequences [18], quantum beats magnetometry [19], multipulse dynamical decoupling [20], and spectral hole burning [21] have been explored. Nonetheless, as it will be detailed, each environmental parameter may act differently depending on the quantum state of the NV center, thus, a thorough analysis of the competition of these parameters in the involved physical process is required. This study will focus on continuous-wave (CW) ODMR and free induction decay (FID) sensing protocols; CW-sensing protocols aim to detect the variation induced by external fields on the resonance frequency of the NV center. Free induction decay

---

[*] Contact author: e.bernardi@inrim.it

sensing protocols measure the phase difference acquired as a consequence of variation in resonance frequency between two components of a quantum superposition. Sensors based on NV centers present a very good sensitivity regarding temperature and magnetic field [22], leading to the possibility of measuring the temperature inside a cell [23–25], magnetic NMR signal coming from a single molecule [26,27] as well as nanoscale imaging of superconducting vortices [28]. Additionally, the NV is widely used in computation applications where paramagnetic ^{13}C nuclei are employed as q bits, the NV center as a mediator q bit, and the neighboring N nucleus as auxiliary q bit [29,30]. Moreover, In recent applications, the possibility of using the network of ^{13}C nuclei for quantum simulation has been investigated [31].

In most of these applications, a bias magnetic field $B_\parallel$ is applied along the NV axis to remove the degeneration of the $S_z = \pm 1$ manifold. In this case, the eigenstates of the system are NV's axial spin eigenstates, namely, $|S_z = +1\rangle$ and $|S_z = -1\rangle$, generally indicated as strong-axial-field states. Conversely, in the presence of a weak magnetic field, electric field, or strain (or a combination) orthogonal to the NV axis (with $B_\parallel = 0$), the eigenstates are balanced linear superposition of the strong-axial-field states: $|+\rangle = \frac{1}{\sqrt{2}}(|S_z = +1\rangle + |S_z = -1\rangle)$ and $|-\rangle = \frac{1}{\sqrt{2}}(|S_z = +1\rangle - |S_z = -1\rangle)$, typically called dressed states [13].

Dressed states have proven to be useful for temperature [32] and electric field measurements [33] since they show a second-order dependency to the magnetic field due to the null spin expectation value for each direction: $\langle +|S_i|+\rangle = \langle -|S_i|-\rangle = 0$ for $i = x, y, z$, leading to longer coherence times [34] when the dominant source of decoherence is magnetic noise [35].

Dressed states have been studied both for single NV center [35–37] and NV ensemble [33,34,38–40]. In the last few years, research has been focusing on the effect of ^{14}N [38] and ^{13}C [37] nuclei on the NV center and their exploitation for electrical field sensing [33,41]. In particular, in the presence of a weak orthogonal field ($B_\perp \neq 0$, $B_\parallel = 0$), it has been shown that two resonances are present for both $|-\rangle$ and $|+\rangle$ [38]. The first is related to the state $I_z^{14N} = 0$, and the other is related to the two degenerate states $I_z^{14\mathrm{N}} = \pm 1$, where $I_z^{14\mathrm{N}}$ is the component of the ^{14}N nuclear spin along the NV axis. This result proves that the NV center interacts with the ^{14}N nucleus despite being almost insensitive to external magnetic fields. The reason is that, as we will discuss later in the paper, for $B_\parallel = 0$, the state with $I_z^{14\mathrm{N}} = 0$ is a balanced superposition of strong-axial-field states, therefore, it is a completely dressed state. The states with $I_z^{14\mathrm{N}} = +1$ and $I_z^{14\mathrm{N}} = -1$, instead, are unbalanced superpositions of the strong-axial-field states with $\langle S_z \rangle > 0$ and $\langle S_z \rangle < 0$, respectively [35], as a result they are more sensitive to the external magnetic field. In this work, these unbalanced superpositions of $|S_z = +1\rangle$ and $|S_z = -1\rangle$ are named partially dressed states. Finally, it should be stressed that applying a weak orthogonal field to observe the interaction between dressed and partially dressed states in the FID decays is unnecessary. This was demonstrated in Ref. [42], where it was shown that the total electric field alone has a similar effect on the eigenenergies of a single NV coupled to a ^{15}N nucleus and is likely to have similar effects on the FID decays. However, employing a weak orthogonal field can enhance the stability of the dressed states by increasing the energy gap, when properly aligned. Additionally, it eliminates the overlap of resonances associated with different orientations of NV's when working with NVs ensembles.

In this paper, via a comprehensive theoretical and experimental investigation of the interplay between dressed and strong-axial-field states in the presence of both a weak orthogonal magnetic field and an electric field (or, equivalently, a strain), it is demonstrated the possibility of simultaneously exciting dressed and partially dressed states. Furthermore, we present an approach consisting of fitting single FID measurements with multiple coherence times, that is of critical importance when working with different classes of states. This methodology will lead to the implementation of two-qubit gates with increased fidelity due to the increased coherence time T_2^* of dressed and partially dressed states, the two qubits will be the electronic spin of the NV center and the nuclear spin of the N atom. Moreover, it could enable a decoupled magnetic field and temperature sensing scheme, operating with limited microwave bandwidth and with a single microwave frequency. In the first part of the work, how strain and weak orthogonal fields compete in forming dressed states is discussed, providing, as a result, the exact eigenstates of the system. Then, FID measurements obtained for two different values of the axial magnetic field are presented, highlighting the presence of dressed and partially dressed states. The study is focused on NV ensembles, but it can be straightforwardly generalized to the single NV center or other solid-state spin systems.

II. THEORETICAL ANALYSIS

The system considered is constituted of NV center electronic spin $\vec{S} = 1$ and ^{14}N nuclear spin $\vec{I} = 1$. The complete Hamiltonian of this system is [13]

$$\begin{aligned}\mathcal{H} = {} & (D_{\mathrm{gs}} + d_\parallel \Pi_\parallel)\left[S_z^2 - \frac{1}{3}S(S+1)\right] \\ & - d_\perp\left[\Pi_x\left(S_x^2 - S_y^2\right) - \Pi_y(S_xS_y + S_yS_x)\right] \\ & + g_e\mu_B B_x S_x + g_e\mu_B B_y S_y + g_e\mu_B B_\parallel S_z \\ & + S_zA_\parallel I_z + S_xA_\perp I_x + S_yA_\perp I_y + Q\left(I_z^2 - \frac{I^2}{3}\right) \\ & + g_n\mu_n B_x I_x + g_n\mu_n B_y I_y + g_n\mu_n B_\parallel I_z, \qquad (1)\end{aligned}$$

where D_{gs} is the ground-state zero-field splitting, $d_\perp$ and $d_\parallel$ are the components of the ground-state electric dipole moment, $\vec{\Pi} = \vec{E} + \vec{\sigma}$ is the total effective electric field that includes both the effect of static electric fields $\vec{E}$ and strain $\vec{\sigma}$ (strain acts as an effective electric field due to the piezoelectric effect). g_e and g_n are electronic and nuclear Landé g factors, μ_B and μ_N are the Bohr and nuclear magneton constants, $\vec{B}$ is the applied magnetic field, $A_\parallel$ and $A_\perp$ describe the hyperfine interaction between $\vec{S}$ and $\vec{I}$, and Q is the nuclear electric quadrupole term.

In Fig. 1(a), the eigenvalues of Hamiltonian in Eq. (1) are numerically evaluated [43] in the presence of a weak

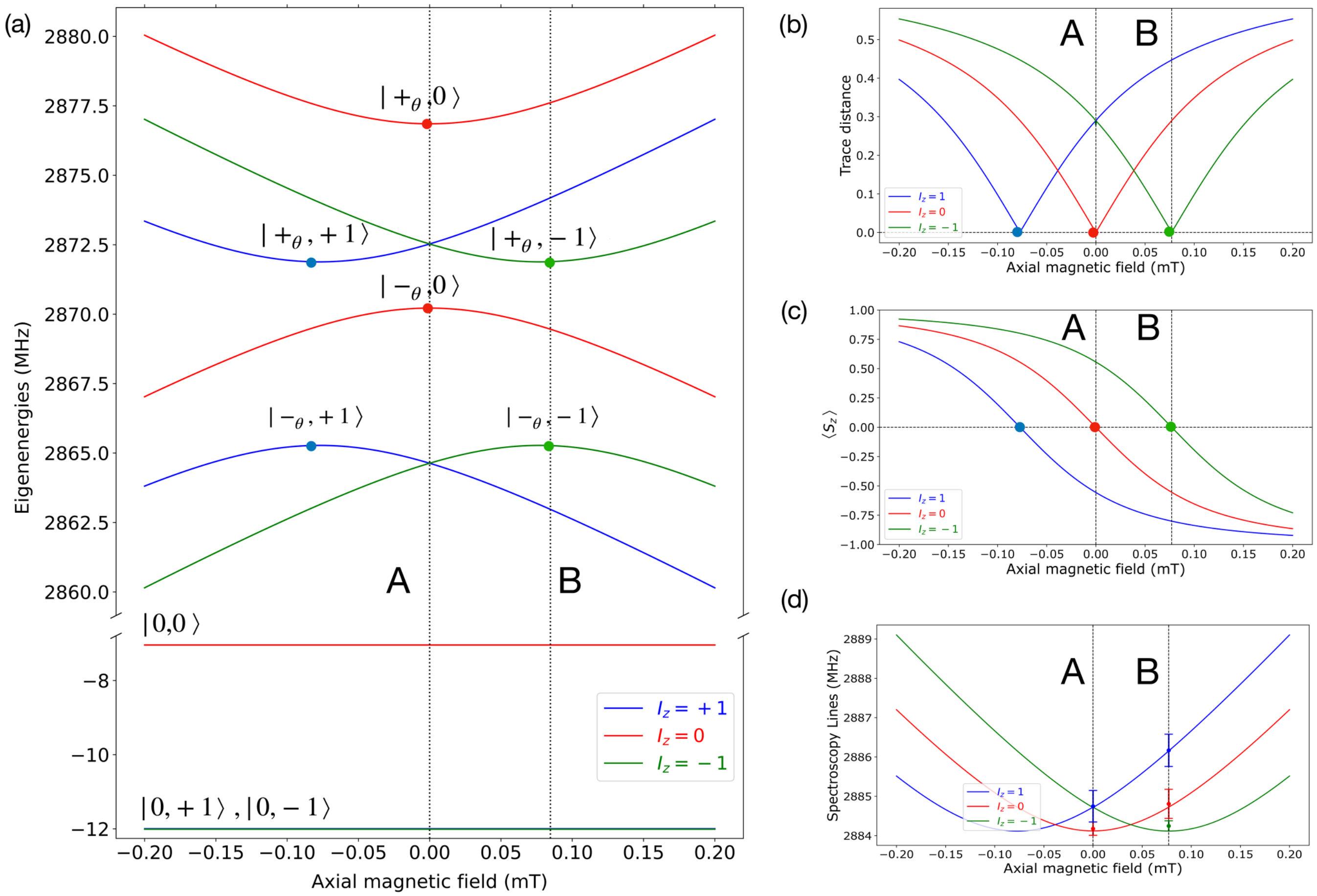

FIG. 1. (a) Exact eigenvalues of Hamiltonian in Eq. (1) as a function of axial magnetic field $B_\parallel$ ($B_\perp$ fixed). The curves are labeled according to the value of the spin eigenstates $|S_z, I_z\rangle$, where S_z and I_z are the axial components of electronic spin and nuclear spin, respectively. In particular, the position of the dressed states $|+_\theta, \cdot\rangle$ and $|-_\theta, \cdot\rangle$ are depicted as small dots. (b) Trace distance between the density matrix derived from electronic dressed state ($|+\rangle_\theta$) and the density matrix derived from the eigenvectors of Eq. (1), as a function of the axial magnetic field $B_\parallel$. (c) Expectation values of S_z on the dressed state eigenvectors $|-_\theta, \cdot\rangle$. (d) Resonance frequencies from $|0\rangle$ to the upper branch of excited states as a function of axial magnetic field $B_\parallel$. The energy differences are computed taking into account selection rules (the applied microwave couples with S_x and S_y, therefore, $\Delta I_z = 0$, $\Delta S_z \pm 1$). The circles represent the resonance frequencies derived from cw-ODMR spectra [see Figs. 2(a) and 3(a)]. The uncertainties in experimental data are the linewidths of the respective ODMR resonances.

fixed orthogonal field $\vec{B_\perp}$ and plotted functions of a varying axial magnetic field $B_\parallel$. This orthogonal field has the form $\vec{B_\perp} = B_x\hat{x} + B_y\hat{y}$, with $B_x = 3.83$ mT and $B_y = 3.33$ mT. Additionally, an orthogonal total electric field $\vec{\Pi_\perp} = \Pi_x\hat{x} + \Pi_y\hat{y}$ is considered, with $\Pi_x = -124\,000$ V cm^{-1} and $\Pi_y = -94\,000$ V cm^{-1}. This term is arising from strain components and static electric field present inside the sample (the values here reported are estimated in agreement with the experimental data, see Supplemental Material [44] and Ref. [45] therein for detailed discussion on the nature and values of this term of the Hamiltonian). In Fig. 1(d) the resonance frequencies as function of the applied field are plotted for the transition $|0\rangle \to |+\rangle$. The resonance frequencies are computed considering the difference in the eigenenergies in Fig. 1(a) and taking into account the selection rules. In the following, the effect of each term in Eq. (1) is analyzed to clarify the nature of the eigenstates, first by describing the effects of electronic interaction terms, and successively by including the nuclear interaction terms also.

A. Electronic interaction terms

We start by considering the case where the nuclear spin interaction terms are neglected. This choice allows to limit the analysis to electron-related terms of the Hamiltonian only, as in Ref. [13]. There, the unperturbed Hamiltonian depends on the ground-state crystal-field splitting D_{gs} while the contributions from the orthogonal total electrical field $\vec{\Pi_\perp}$ and the orthogonal field $\vec{B_\perp}$ are considered as perturbations, developing the perturbative solution up to the second order in eigenenergies (the effect of parallel strain $\Pi_\parallel$ is negligible because $d_\parallel \ll d_\perp$). In the present analysis, instead, the exact eigenstates are computed by diagonalization of the partial Hamiltonian containing only the electronic spin terms (zero field, magnetic field, electric field). Then, the newly obtained eigenstates and eigenenergies are expressed as a truncated power series of the parameter $\zeta = \frac{g_e\mu_B B_\perp}{D_{\text{gs}}}$(for detailed calculations see Appendix A).

The effect of D_{gs} is to create a large gap between the eigenenergy $E_{|S_z=0\rangle}$, relative to the eigenstate $|S_z = 0\rangle$, and the eigenenergies $E_{|-\rangle} = E_{|+\rangle}$ relative to the two degenerate states $|-\rangle$ and $|+\rangle$. The combined contribution of the total orthogonal electric field $\vec{\Pi}_\perp$ and weak orthogonal field $\vec{B}_\perp$ can be summarized in four effects:

(i) Rotate the original dressed states $|0\rangle, |-\rangle, |+\rangle$ of an angle θ along the z axis, giving the eigenstates $|0\rangle_\theta, |-\rangle_\theta, |+\rangle_\theta$, with

$$\theta = \tfrac{1}{2}\arg(e^{2i\phi_{B_\perp}} - 2\,\mathrm{R}e^{-i\phi_\Pi}). \tag{2}$$

(ii) Create an energy gap between $|-\rangle_\theta$ and $|+\rangle_\theta$, where

$$E_{\mathrm{gap}} = 2\left[\left(\frac{\mathcal{B}_\perp^2}{2D_{\mathrm{gs}}}\right)^2 + \mathcal{E}^2 - \mathcal{E}\frac{\mathcal{B}_\perp^2}{D_{\mathrm{gs}}}\cos(2\phi_{B_\perp} + \phi_\Pi)\right]^{\frac{1}{2}}. \tag{3}$$

(iii) Create a small mixing, proportional to $\frac{\mathcal{B}_\perp}{D_{\mathrm{gs}}}$, between $|+\rangle_\theta, |-\rangle_\theta$, and $|0\rangle$.

(iv) Decrease the energy of the $|0\rangle$ state to $E_0 = -\frac{\mathcal{B}_\perp^2}{D_{\mathrm{gs}}} < 0$.

The following quantities are introduced:

$$\mathcal{B}_\perp = g_e\mu_B B_\perp\,, \quad \mathcal{E} = d_\perp\Pi_\perp\,, \quad R = \frac{\mathcal{E}D_{\mathrm{gs}}}{\mathcal{B}_\perp^2}, \tag{4}$$

and

$$\phi_\Pi = \arctan\left(\frac{\Pi_y}{\Pi_x}\right), \quad \phi_{B_\perp} = \arctan\left(\frac{B_y}{B_x}\right). \tag{5}$$

The explicit expression of the rotated eigenstates is (for the detailed theoretical model, see Appendix A)

$$\begin{aligned}
|0\rangle_\theta &= |0\rangle,\\
|-\rangle_\theta &= \frac{1}{\sqrt{2}}(e^{-i\theta}|S_z = +1\rangle - e^{i\theta}|S_z = -1\rangle),\\
|+\rangle_\theta &= \frac{1}{\sqrt{2}}(e^{-i\theta}|S_z = +1\rangle + e^{i\theta}|S_z = -1\rangle).
\end{aligned} \tag{6}$$

It is significant to study the dependency between θ and R, which are the rotation angle of dressed states and the relative magnitude of $\Pi_\perp$ and $B_\perp$, respectively, since the latter is defining how dressed states are aligned with respect to bias electric and magnetic fields. First, we consider the two limit cases for R. On the one hand, when the contribution of the orthogonal magnetic field $B_\perp$ is dominant ($R \sim 0$), the eigenstates are rotated by $\phi_{B_\perp}$, i.e., are aligned along the direction of $B_\perp$. On the other hand, when the contribution from the total orthogonal electric field Π is dominant ($R \gg 1$), the original eigenstates $|0\rangle, |-\rangle, |+\rangle$ are rotated by $\frac{\pi}{2} - \phi_\Pi/2$. For intermediate values of R, the competition between the orthogonal magnetic field $B_\perp$ and the orthogonal total electric field $\Pi_\perp$ results in a intermediate rotation between $\phi_{B_\perp}$ and $\frac{\pi}{2} - \phi_\Pi/2$, determined by the relative magnitude of $B_\perp$ and $\Pi_\perp$. The general expression of θ shown in Eq. (2) represents the first result of this paper.

Figure 1(b) shows the trace distances [46,47] between the state $|+\rangle_\theta$ and the numerically evaluated eigenstates of the Hamiltonian in Eq. (1) as a function of the axial field $B_\parallel$. For the moment, we consider only the data regarding nuclear spin $I_z = 0$ (red curve) because we are neglecting the effect of the nuclear spin. The data indicate that the two states are at zero distance for $B_\parallel = 0$. This means that the eigenvectors in Eqs. (6) are still dressed states, i.e., a balanced superposition of strong-axial-field states, and the small mixing between $|+\rangle_\theta$ and $|0\rangle$ is negligible, for our experimental conditions. Being the eigenstates balanced superposition of strong-axial-field states, they are sensitive to the field $\vec{B}$ only at second order since

$$_\theta\langle S_z = 0|S_i|S_z = 0\rangle_\theta =_\theta \langle -|S_i|-\rangle_\theta =_\theta \langle +|S_i|+\rangle_\theta = 0 \quad \text{for } i = x, y, z. \tag{7}$$

Figure 1(c) shows $\langle S_z\rangle$ in function of the axial field $B_\parallel$ and it can be noticed that $\langle S_z\rangle = 0$ for $B_\parallel = 0$, as predicted by Eq. (7).

By introducing a small axial magnetic field $\mathcal{B}_\parallel^2 < (E_{\mathrm{gap}}/2)^2$ and neglecting the minor mixing of $|+\rangle_\theta, |-\rangle_\theta$ with $|0\rangle$, the calculated eigenvectors become

$$\begin{aligned}
|-\rangle_{\theta,\mathcal{B}_\parallel} &= \sin\left(\frac{\gamma}{2}\right)e^{-i\theta}|S_z = +1\rangle - \cos\left(\frac{\gamma}{2}\right)e^{i\theta}|S_z = -1\rangle,\\
|+\rangle_{\theta,\mathcal{B}_\parallel} &= \cos\left(\frac{\gamma}{2}\right)e^{-i\theta}|S_z = +1\rangle + \sin\left(\frac{\gamma}{2}\right)e^{i\theta}|S_z = -1\rangle,
\end{aligned} \tag{8}$$

while the corresponding eigenergies are

$$\begin{aligned}
E_0^{(2)} &= -\frac{\mathcal{B}_\perp^2}{D_{\mathrm{gs}}},\\
E_{-,\theta,\mathcal{B}_\parallel}^{(2)} &= D_{\mathrm{gs}} + \frac{\mathcal{B}_\perp^2}{2D_{\mathrm{gs}}} - \sqrt{(E_{\mathrm{gap}}/2)^2 + \mathcal{B}_\parallel^2},\\
E_{+,\theta,\mathcal{B}_\parallel}^{(2)} &= D_{\mathrm{gs}} + \frac{\mathcal{B}_\perp^2}{2D_{\mathrm{gs}}} + \sqrt{(E_{\mathrm{gap}}/2)^2 + \mathcal{B}_\parallel^2}
\end{aligned} \tag{9}$$

with $\mathcal{B}_\parallel = g_e\mu_B B_\parallel$ and $\tan\gamma = \frac{E_{\mathrm{gap}}}{2\mathcal{B}_\parallel}$ (see Appendix A for a derivation of these equations).

For $\mathcal{B}_\parallel = 0$, one has $\frac{\gamma}{2} = \frac{\pi}{4}$, therefore, the eigenstates are balanced superpositions of strong-axial-field states. As $\mathcal{B}_\parallel$ increases, $\frac{\gamma}{2}$ decreases, therefore, the states become partially dressed states and acquire a nonzero value of $\langle S_z\rangle$. For larger axial magnetic fields $[\mathcal{B}_\parallel^2 \gg (\frac{E_{\mathrm{gap}}}{2})^2]$ the eigenergies become linear in $B_\parallel$ resulting in strong-axial-field states. This behavior can be seen in Fig. 1(a). Moreover, as $B_\parallel$ increases, the trace distance between the states also increases in Fig. 1(b). Additionally, with increasing $B_\parallel$ the eigenstates acquire a nonzero value of $\langle S_z\rangle$ [Fig. 1(c)], as predicted by Eqs. (8).

B. Complete Hamiltonian

The interaction between NV electronic spin and ^{14}N nuclear spin $\vec{I}$ comprises two terms, quadrupolar and hyperfine interactions. The effect of the quadrupolar term is to turn I_z into a good quantum number and to increase the energy of states with $I_z = \pm 1$. The effect of the hyperfine term is well known; it shifts the position of the dressed state from ${B_\parallel}^{\mathrm{dressed}} = 0$ to ${B_\parallel}^{\mathrm{dressed}} = \mp\frac{A_\parallel}{g_e\mu_B}$ for $I_z = \pm 1$. This phenomenon enables the simultaneous presence of dressed and partially dressed for the same applied field $B_\parallel$.

The analysis of the complete Hamiltonian eigenenergies will focus on two values of $B_\parallel$:

(i) $B_\parallel = 0$ (point A in Fig. 1). At this point, the eigenstates with $I_z = 0$ are dressed states, the eigenstates with $I_z = \pm 1$

are degenerate partially dressed states, with opposite values of $\langle S_z \rangle$ [48].

(ii) $B_\parallel = \frac{A_\parallel}{g_e \mu_B}$ (point B in Fig. 1). At this point, the eigenstate with $I_z = -1$ is completely dressed, and the two other eigenstates are partially dressed.

As it will be discussed later, working in point A is promising for quantum computation applications, and working in point B is promising for quantum sensing applications.

III. EXPERIMENTAL RESULTS AND DISCUSSION

Our experimental investigation was performed on an ensemble of $N \sim 6 \times 10^4$ independent NV centers distributed in a volume $V \sim 1 \times 10^{-17}$ m^3 (see Supplemental Material [44]). Each NV is subjected to inhomogeneous magnetic and total effective electric fields, described by the distributions $f_B(B)$ and $f_\Pi(\Pi)$. By reasonably neglecting the interaction between NV centers, the experimental results can be interpreted by solving Eq. (1) for each value of B and Π. The eigenstate of the ensemble is the tensor product of the single NV density matrices, with each density matrix weighted according to $f_B(B)$ and $f_\Pi(\Pi)$. The eigenenergies of the ensemble are the weighted sum of a single NV eigenergies according to $f_B(B)$ and $f_\Pi(\Pi)$. The resonant frequency ν_{res}, which is computed from the differences in the eigenergies, also follows a distribution $f_{\nu_{\text{res}}}(\nu_{\text{res}})$. In the following, two sets of results are presented: the first is related to CW microwave excitation, and the second to pulsed measurements (i.e., FID). In both cases we consider only the upper branch of Fig. 1(a), i.e., the transition from $|0\rangle$ to $|+\rangle_\theta$.

A. Cw excitation

In a CW-ODMR measurement [see Figs. 2(a) and 3(a)], an oscillating magnetic field with frequency ν_{MW} and a 532-nm laser are applied simultaneously, exploiting a conventional single-photon confocal microscope with the light detected by a single-photon detector (see [49] and Supplemental Material [44] and Refs. [50,51] therein for details on the experimental setup). The laser excitation has two effects: (i) inducing red photoluminescence (PL), whose intensity depends on the spin state of the NV, with $|0\rangle$ being brighter than $|-\rangle_\theta$ and $|+\rangle_\theta$; and (ii) polarizing the NV in spin state $|0\rangle$. To explain the technique, let us focus on states $|0\rangle$ and $|+\rangle_\theta$. If ν_{MW} is far from the resonant frequency $\nu_{\text{res}} = (E_{|0\rangle} - E_{|+\rangle_\theta})/\hbar$, the oscillating magnetic field is not effective in driving transitions between $|0\rangle$ and $|+\rangle_\theta$, moreover, the green light polarizes the NV state to $|0\rangle$, resulting in brighter PL emission. Conversely, when $\nu_{\text{MW}} = \nu_{\text{res}} = (E_{|0\rangle} - E_{|+\rangle_\theta})/\hbar$, the oscillating field is very effective in driving transitions between $|0\rangle$ and $|+\rangle_\theta$, therefore, the dark state $|+\rangle_\theta$ is populated and the collected PL presents a minimum [52].

In Fig. 1 (point A), two resonances are observable for $B_\parallel = 0$, one related to a dressed state, $\nu_{A,\text{dres}}$, and the other, $\nu_{A,\text{p-dres1}}$, related to two degenerate partially dressed states with opposite values of $\langle S_z \rangle$, as predicted numerically [see Figs. 1(c) and 1(d)]. The two transitions are visible in the ODMR spectrum in Fig. 2(a), the difference $\Delta_{0,\text{cw}} = \nu_{A,\text{dres}} - \nu_{A,\text{p-dres1}}$ between the two resonance frequencies is indicated. By fitting the two resonances we note that the resonance corresponding to $I_z = \pm 1$ presents a double contrast with respect to the one corresponding to $I_z = 0$, due to the presence of the two degenerate populations. In point B, for $B_\parallel = \frac{A_\parallel}{g_e \mu_B}$, there are three resonant frequencies: one corresponding to a dressed state, $\nu_{B,\text{dres}}$, and two corresponding to partially dressed states with different nonzero values of $\langle S_z \rangle$, $\nu_{B,\text{p-dres2}}$ $(I_z = 0)$ and $\nu_{B,\text{p-dres3}}$ $(I_z = +1)$. The three resonances are visible in the ODMR spectrum in Fig. 3(a). In this case, the fitting results suggest that resonances present similar contrasts, as expected since each resonance corresponds to a single state. Actually, the resonance belonging to the partially dressed state with $I_z = +1$ presents a slightly lower contrast since we use a linearly polarized oscillating field that is less effective to drive strongly unbalanced partially dressed states (see discussion below). The three frequency differences $\Delta_{1,\text{cw}} = \nu_{B,\text{dres}} - \nu_{B,\text{p-dres2}}$, $\Delta_{2,\text{cw}} = \nu_{B,\text{p-dres2}} - \nu_{B,\text{p-dres3}}$, and $\Delta_{3,\text{cw}} = \nu_{B,\text{dres}} - \nu_{B,\text{p-dres3}}$ are indicated. It is important to underline that $\nu_{A,\text{dres}} = \nu_{B,\text{dres}}$ because in point B the axial field compensates the hyperfine term, while the contribution of the nuclear quadrupolar term is equivalent both for $|0, 1\rangle$ and $|+_\theta, 1\rangle$. Therefore, it does not enter into the derivation of $\nu_{B,\text{dres}}$.

The different states are excited by different polarizations of the oscillating field. Considering Rabi and FID measurements, the dressed state $|+_\theta\rangle$ $(|-_\theta\rangle)$ is excited by an oscillating magnetic field which is linearly polarized in the x-y plane and aligned along the direction defined by the angle θ $(\theta + \frac{\pi}{2})$ in Eq. (2). The strong-axial-field state $|+1\rangle$ $(|-1\rangle)$ is excited by an oscillating magnetic field that is circularly counterclokwise (clockwise) polarized in the x-y plane, and that can be viewed as the balanced sum of two oscillating fields linearly polarized along orthogonal directions. Partially dressed states $|+\rangle_{\theta,\mathcal{B}_\parallel}$, $|-\rangle_{\theta,\mathcal{B}_\parallel}$, for the same $\mathcal{B}_\parallel$, are excited by oscillating magnetic fields elliptically polarized in the x-y plane with reciprocal ellipticity and opposite rotation direction. See Appendix C for further details.

An oscillating magnetic field linearly polarized in the x-y plane along an angle different from θ is used. This allows us to excite dressed states, strong-axial-field states, and partially dressed states: This oscillating magnetic field can be viewed as the sum of two linearly polarized fields, one polarized along θ and the other in a direction orthogonal to θ. In this way we can excite both $|+_\theta\rangle$ and $|-_\theta\rangle$. The linearly polarized oscillating magnetic field can also be viewed as the sum of a countercolockwise and a clockwise circularly polarized fields. In this way we can excite both $|+1\rangle$ and $|-1\rangle$. Furthermore, the linearly polarized oscillating magnetic field can also be viewed as the sum of elliptically polarized fields of reciprocal ellipticity and opposite rotation directions [53]. In this way we can excite both $|+\rangle_{\theta,\mathcal{B}_\parallel}$ and $|-\rangle_{\theta,\mathcal{B}_\parallel}$. In the experimental conditions of this work, the linear oscillating magnetic field is along an angle intermediate between θ and $\theta + \frac{\pi}{2}$, and all the transitions are driven with similar strength. We underline that, in general, the strength of the driving is different for the dressed states, partially dressed states, and strong-axial-field states.

CW-ODMR spectra hint at the different behaviors of dressed and partially dressed states. Notably, the former ones exhibit narrower transition linewidths with respect to the latter ones. This is because the dressed states are sensitive only at the second order to noise coming from coupling with the spin

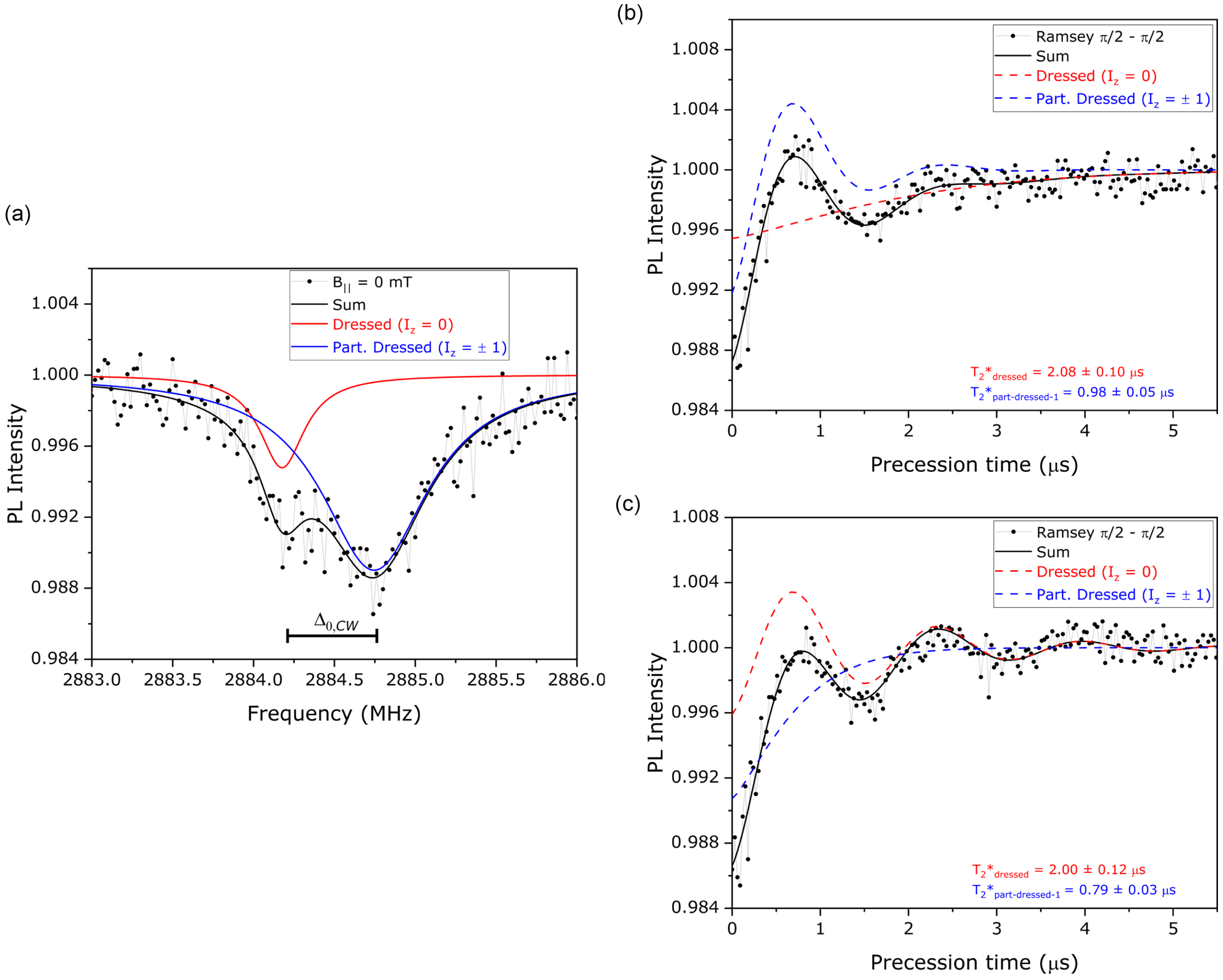

FIG. 2. Experimental results for $B_\parallel = 0$, corresponding to point A of Fig. 1(a) upper branch: (a) optically detected magnetic resonance spectra. Two resonances are present. The blue solid line fits the one related to the two degenerate partially dressed states ($I_z = \pm 1$), following a Lorentzian distribution. The red solid line fits the one related to the dressed state ($I_z = 0$). The black curve corresponds to the sum of the two Lorentzians. (b) Free induction decay relaxation for a microwave of frequency $\nu_{\rm MW} = \nu_{A,\rm dres}$ on resonance with the dressed state $I_z = 0$. The decay is fitted as the contribution of a pure stretched exponential, red dashed curve, relative to the dressed state $I_z = 0$, and an oscillating stretched exponential, blue dashed curve, related to the partially dressed states with $I_z = \pm 1$. (c) Free induction decay relaxation for a microwave of frequency $\nu_{\rm MW} = \nu_{A,\text{p-dres1}}$ on resonance with the degenerate partially dressed states $I_z = \pm 1$. The decay is fitted as the contribution of a pure stretched exponential, blue dashed curve, related to the partially dressed states with $I_z = \pm 1$, and an oscillating stretched exponential, red dashed curve, related to the dressed state with $I_z = 0$. In all curves, the value of the stretched exponential is fixed to $p = 1.28$, derived from the fit of the decaying of strong-axial-field states (see Supplemental Material [44]).

baths and spatial inhomogeneities and temporal fluctuations in the external magnetic field B. When these are the two main sources of decoherence, dressed states are expected to show longer coherence times T_2^* (see Appendixes D and E). CW-ODMR measurements are not ideal for discriminating between dressed and partially dressed states due to the effect of power broadening: to clearly resolve peaks linked to the different states, it is necessary to decrease the microwave (MW) power. However, this decreases the contrast and reduces the overall S/N ratio. Hence, FID measurements are selected to characterize the different types of states since these are not affected by MW-power broadening and can give a direct evaluation of T_2^*.

B. Pulsed measurements

In general, FID measurement procedures consist in an initialization optical pulse, two $\frac{\pi}{2}$ MW pulses separated by a free precession interval of duration τ and a final readout optical pulse (see Supplemental Material [44] and Ref. [54] therein). The system is initialized in the state $|0\rangle$, the first $\frac{\pi}{2}$ pulse brings the state in a superposition of $|0\rangle$ and $|S_z \neq 0\rangle$. During the free evolution time, the two components of the superposition acquire a phase difference ϕ depending on the detuning $\Delta = \nu_{\rm MW} - \nu_{\rm res}$ between MW excitation frequency $\nu_{\rm MW}$ and the resonant frequency $\nu_{\rm res}$. The second $\frac{\pi}{2}$ encodes ϕ in the population of the $|0\rangle$ state ($p_{|0\rangle}$) [54]. The final read-out optical pulse excites a PL proportional to $p_{|0\rangle}$. The general

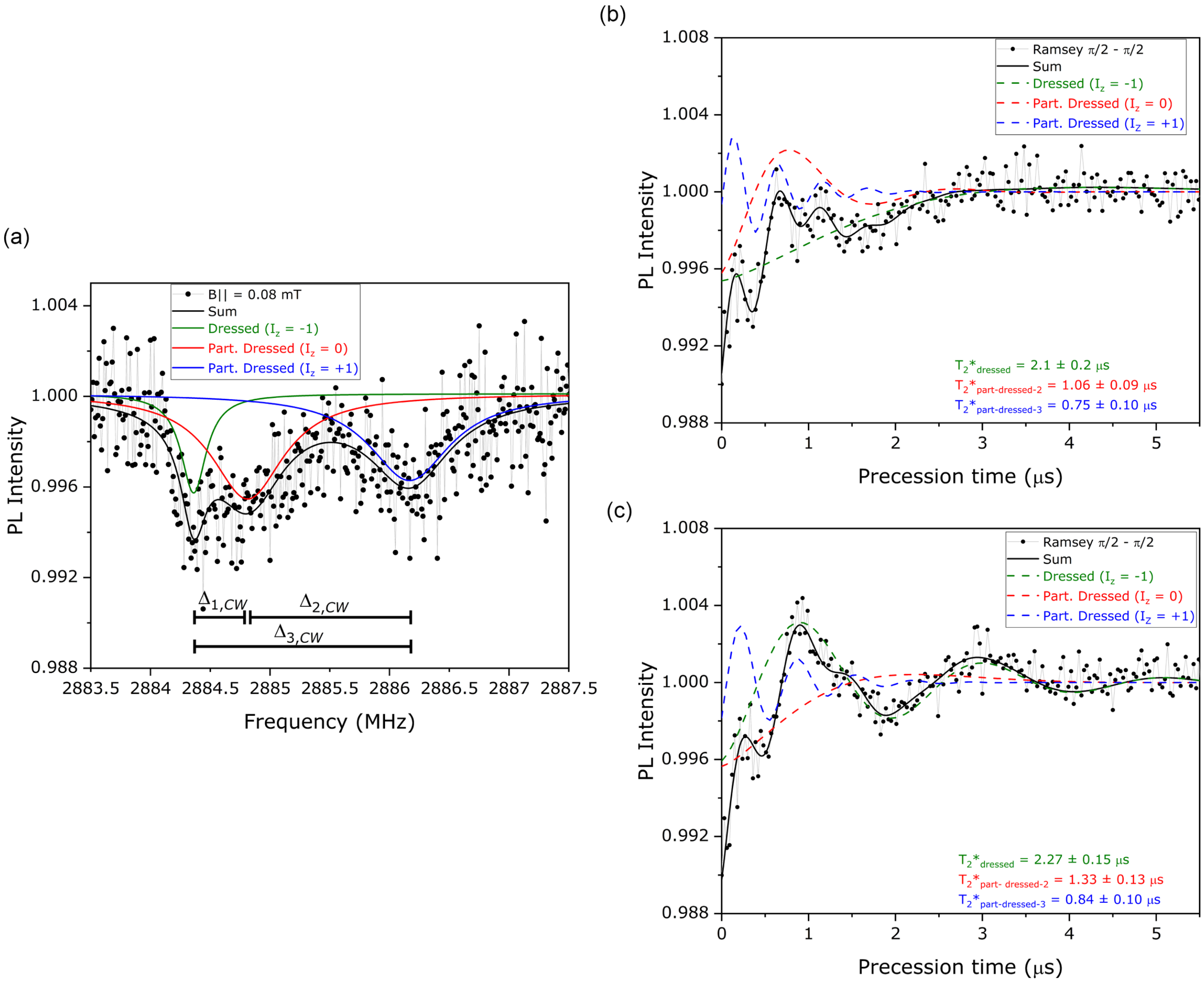

FIG. 3. Experimental results for $B_\parallel = 0.8$ mT, corresponding to point B of Fig. 1(a) upper branch: (a) optically detected magnetic resonance spectrum. Three resonances are present. The blue solid line fits the resonance related to a partially dressed state ($I_z = +1$). The red solid line fits the resonance related to another partially dressed state ($I_z = 0$). The one at the larger frequency $\nu_{B,\mathrm{dres}}$ is related to the dressed state ($I_z = -1$). The green solid line fits this resonance following a Lorentzian distribution. (b) Free induction decay relaxation for a microwave of frequency $\nu_{\mathrm{MW}} = \nu_{B,\mathrm{dres}}$ on resonance with the dressed state $I_z = -1$. The decay is fitted as the contribution of a very slow oscillating stretched exponential, green dashed curve, and two faster oscillating stretched exponentials, red dashed curve and blue dashed curve. The very slow stretched exponential is related to the dressed state with $I_z = -1$. The intermediate oscillating exponential is related to the partially dressed state with $I_z = 0$. The faster oscillating exponential is related to the partially dressed state with $I_z = +1$. (c) Free induction decay relaxation for a microwave of frequency $\nu_{\mathrm{MW}} = \nu_{B,\mathrm{p\text{-}dres2}}$ on resonance with the dressed state $I_z = 0$. The decay is fitted as the contribution of a pure stretched exponential, red dashed curve, and two oscillating stretched exponentials, green dashed curve and blue dashed curve. The pure stretched exponential is related to the partially dressed state with $I_z = 0$. The slower oscillating exponential is related to the dressed state with $I_z = -1$, and the faster oscillating exponential is related to the partially dressed state with $I_z = +1$. The value of the stretched exponential is fixed to $p = 1.28$, derived from the fit of the decaying of strong-axial-field states.

form of $p_{|0\rangle}$ for a FID measurement where a single resonance is driven is

$$p_{|0\rangle}(\tau) = \tfrac{1}{2}\left[1 - e^{-(\frac{\tau}{T_2^*})^p}\cos(2\pi\Delta\tau)\right] \qquad (10)$$

with $1 \leqslant p < 2$, where we neglect the effect of the detuning during the $\frac{\pi}{2}$ pulses. The coherence time T_2^* defines the timescale at which the system loses quantum coherence, and $p_{|0\rangle}$ decays to $\frac{1}{2}$, corresponding to a completely mixed state [55]. For an ensemble of NVs, the decay is caused by different sources of decoherence: coupling with surrounding spins, temporal fluctuations, and spatial gradients in the external fields B_i and Π_i [56,57]. The value of p provides information on the relative weight of the different sources of decoherence: if $p \sim 1$ the main source of decoherence is coupling with surrounding spins, while an increase in p corresponds to a greater influence of temporal fluctuations and spatial gradients of the external fields [56–58].

To fit the experimental FID's, the expression in Eq. (10) has to be modified taking into account a FID contrast $A < 1$ and the effect of the detuning during the $\frac{\pi}{2}$ pulses. Furthermore, if

TABLE I. Values of coherence time T_2^*, derived from the fit of the free induction decays for different experimental conditions. Each row corresponds to a value of axial field $B_\parallel$ and of microwave frequency ν_{MW}.

	T_2^* dressed (μs)	T_2^* part-dressed-1 (μs)	T_2^* part-dressed-2 (μs)	T_2^* part-dressed-3 (μs)	T_2^* Strong axial field (μs)
$B_\parallel = 0(\mathrm{A}),\ \nu_{\mathrm{MW}} = \nu_{A,\mathrm{dres}}$	2.08 ± 0.10	0.98 ± 0.05			
$B_\parallel = 0(\mathrm{A}),\ \nu_{\mathrm{MW}} = \nu_{A,\text{p-dres1}}$	2.00 ± 0.12	0.79 ± 0.03			
$B_\parallel = \frac{A_\parallel}{g_e\mu_B}(\mathrm{B}),\ \nu_{\mathrm{MW}} = \nu_{B,\mathrm{dres}}$	2.1 ± 0.2		1.06 ± 0.095	0.75 ± 0.18	
$B_\parallel = \frac{A_\parallel}{g_e\mu_B}(\mathrm{B}),\ \nu_{\mathrm{MW}} = \nu_{B,\text{p-dres2}}$	2.27 ± 0.15		1.33 ± 0.13	0.84 ± 0.11	
Strong axial field					$0.66. \pm 0.09$

the microwave pulse $\frac{\pi}{2}$ has enough spectral width [59] to drive more than one resonance, the PL signal is the sum of multiple terms with different $\Delta_i = \nu_{\mathrm{MW}} - \nu_{\mathrm{res},i}$. The final expression for each transition in the FID is

$$y_i(t) = \frac{1}{2}\left[1 - \frac{A}{y_0}\frac{\Omega^2}{\Omega^2 + \Delta_i^2} \times \cos\left[\Delta_i t + 2\arcsin\left(\frac{\Delta_i}{\Omega}\right)\right] e^{-(\frac{t}{T_{2,i}^*})^p}\right], \tag{11}$$

where A is the FID contrast for the transition with $\Delta = 0$, y_0 is the normalization factor, and Ω is the Rabi frequency (see Supplemental Material [44] for complete derivation of the analytical function). We underline that in Eq. (11) the presence of the initial phase and a factor $\frac{\Omega^2}{\Omega^2+\Delta_i^2}$ contribute both to the reduction of the measured contrast when $\Delta_i \neq 0$.

The first set of pulsed measurements (Fig. 2) was collected with $B_\parallel = 0$, corresponding to point A in Fig. 1. The spectral width is sufficient to excite both resonances. First, we consider a FID measurement on resonance with the dressed state with $I_z = 0$, $\nu_{\mathrm{MW}} = \nu_{A,\mathrm{dres}}$, shown in Fig. 2(b). The experimental curve is as the sum of a pure stretched exponential and an oscillating stretched exponential

$$\begin{aligned} y_{A1} &= y_{A1,I_z=0} + y_{A1,I_z\pm1}, \\ y_{A1,I_z=0}(t) &= \frac{1}{2}\left[1 - \frac{A_{A1}}{y_{0,A1}} e^{-(\frac{t}{T_2^*{}_{\mathrm{dressed},I_z=0}})^p}\right], \\ y_{A1,I_z\pm1}(t) &= \frac{1}{2}\left[1 - 2\frac{A_{A1}}{y_{0,A1}}\frac{\Omega^2}{\Omega^2 + \Delta_{0,A1,\mathrm{FID}}^2} \times \cos\left[\Delta_{0,A1,\mathrm{FID}} t + 2\arcsin\left(\frac{\Delta_{0,A1,\mathrm{FID}}}{\Omega}\right)\right] \times e^{-(\frac{t}{T_2^*{}_{\text{part-dressed-1},I_z\pm1}})^p}\right]. \end{aligned} \tag{12}$$

The pure stretched exponential is associated with no detuning, corresponding to the resonance of the dressed state. The oscillating exponential is associated with a detuning $\Delta_{0,A1,\mathrm{FID}} = 565$ kHz, corresponding to the resonance of the degenerate partially dressed states. The factor 2 in the expression of $y_{I_z\pm1}(t)$ is due to the degeneration of the resonance. The estimated coherence time of dressed states is two times longer than that of the partially dressed state, as listed in Table I.

A similar improvement in T_2^* is observed when the FID measurement is performed on resonance with the degenerate partially dressed states with $I_z = \pm1$, $\nu_{\mathrm{MW}} = \nu_{A,\text{p-dres1}}$, as shown in Fig. 2(c). Also in this case the experimental curve is the sum of a pure stretched exponential and an oscillating stretched exponential. But now the oscillating exponential is related to the dressed state, and the pure exponential to the partially dressed states:

$$\begin{aligned} y_{A2} &= y_{A2,I_z=0} + y_{A2,I_z\pm1}, \\ y_{A2,I_z=0}(t) &= \frac{1}{2}\left[1 - \frac{A_{A2}}{y_{0,A2}}\frac{\Omega^2}{\Omega^2 + \Delta_{0,A2,\mathrm{FID}}^2} \times \cos\left[\Delta_{0,A2,\mathrm{FID}} t + 2\arcsin\left(\frac{\Delta_{0,A2,\mathrm{FID}}}{\Omega}\right)\right] \times e^{-(\frac{t}{T_2^*{}_{\mathrm{dressed},I_z=0}})^p}\right], \\ y_{A2,I_z\pm1}(t) &= \frac{1}{2}\left[1 - \frac{A_{A2}}{y_{0,A2}} e^{-(T_2^*{}_{\text{part-dressed-1},I_z\pm1})^p}\right]. \end{aligned} \tag{13}$$

Moreover, the values of T_2^* for dressed states are compatible among measurements performed on resonance with different transitions. This behavior can also be observed for the values of T_2^* for partially dressed states. A quick observation of the experimental decays in Fig. 2 confirms the previous finding: oscillations last longer when the detuned state is the dressed state. The detunings $\Delta_{0,A1,\mathrm{FID}}$, $\Delta_{0,A2,\mathrm{FID}}$ are quite close to each other and are compatible with $\Delta_{0,\mathrm{cw}}$ (see Supplemental Material [44] for the complete discussion of the fit parameters) previously derived from continuous-wave measurements. The contrast coefficients A_{A1} and A_{A2} have almost the same value; this means that the difference in the driving strength due to polarization for dressed and partially dressed states can be considered negligible (see Supplemental Material [44]).

FID measurements were also conducted for another subensemble with a different NV-axis orientation, as detailed in the Appendix F, that exhibited a component along the z axis $B_\parallel \approx 3$ mT. The FID data were recorded by tuning the MW frequency on resonance with the central hyperfine peak, thus, only a single detuning ($\nu = 2.16$ MHz) is observed (see Fig. 5). As described in the previous section, strong-axial-field states couple with the spin bath and fluctuations of external magnetic fields, leading to shorter coherence times than dressed states. In this case, the axial field is much larger than the orthogonal field, therefore, the eigenstates are pure strong-axial-field states, resulting in T_2^* that is more than two times shorter than the one obtained for dressed states, as shown in Table I.

Dressed states, partially dressed states, and strong-axial-field states present different coherence times as they are affected differently by the various sources of decoherence. Dressed states are more sensitive to temporal fluctuation and inhomogeneities of the total electric field $\vec{\Pi}$ because $\langle S_x^2 - S_y^2\rangle \neq 0$, $\langle S_xS_y + S_yS_x\rangle \neq 0$ which are the coupling terms for Π_x and Π_y in the Hamiltonian presented in Eq. (1), while $\langle S_z\rangle = 0$. Strong-axial-field states are more sensitive to dipolar coupling with the surrounding spin bath, temporal fluctuation, and spatial gradients of the axial magnetic field $B_\parallel$ because $\langle S_z\rangle \neq 0$ while $\langle S_x^2 - S_y^2\rangle$, $\langle S_xS_y + S_yS_x\rangle = 0$. On the other hand, for partially dressed state, $\langle S_z\rangle \neq 0$ and $\langle S_x^2 - S_y^2\rangle$, $\langle S_xS_y + S_yS_x\rangle \neq 0$, therefore, the different sources of decoherence compete. For more details on this topic, see [35] and Appendix E. The decrease in coherence time T_2^* observed when passing from dressed states to partially dressed states then to strong-axial-field states indicates that dipolar coupling with surrounding spin baths and temporal fluctuations and spatial inhomogeneities of the axial magnetic field are the major sources of decoherence in the sample being studied. This can be explained by the high concentration of ^{14}N spin centers that couple to NVs as a consequence of the large implantation fluence employed ($F = 1 \times 10^{14}$ cm^{-2}). The stretched exponential parameter p should differ for dressed, partially dressed, and strong-axial-field states. Dressed states are more influenced by inhomogeneities and temporal fluctuations of $\vec{\Pi}$; therefore, a value of p close to 2 is expected. For strong-axial-field states, instead, a value of p close to 1 is expected due to the effect of the spin bath. In general, the value of p is set by the competition between these decoherence sources and the values of field gradients. For simplicity, the value $p = 1.28$ obtained from the single decay of strong-axial field states is used as a fixed parameter for decays of both dressed and partially dressed states, taking into account that a considerable uncertainty is associated with the estimation of p (see Supplemental Materials [44]).

The main result of this work is described by the experimental data shown in Fig. 2, which clearly indicate the ability to coherently drive two resonance states associated with different values of the nuclear spin I_z, while extending the coherence time T_2^* with respect to the typically used strong-axial-field state. This opens up the potential for leveraging the weak orthogonal field regime to achieve high-fidelity C$_n$NOT$_e$ gates, which are essential for quantum computation and have also been recently employed to enhance the sensitivity of magnetic measurements [60]. A basic C$_n$NOT$_e$ gate can be realized by employing the FID sequence on resonance with the dressed state with $I_z = 0$, and adjusting the free evolution time to $\tau = \frac{\pi}{\Delta}$, which corresponds to the half-period of the decaying oscillations.

In more detail, if we start from the state $|S_z = 0\rangle \otimes |I_z = 0\rangle$, at the end of the FID sequence, we will have the state $|S_z = -\rangle \otimes |I_z = 0\rangle$. We are on resonance, and so the superposition $(|S_z = 0\rangle + |S_z = -\rangle) \otimes |I_z = 0\rangle$, created by the first $\frac{\pi}{2}$, does not precede, but it is only subjected to dephasing. The second $\frac{\pi}{2}$ pulse creates the state $|S_z = -\rangle \otimes |I_z = 0\rangle$, if we neglect the dephasing. The FID sequence acts as a π pulse. Instead, if we start from the state $|S_z = 0\rangle \otimes (|I_z = +1\rangle + |I_z = -1\rangle)$, the first $\frac{\pi}{2}$ pulse creates the superposition $(|S_z = 0\rangle + |S_z = -_{\theta,B_\parallel}\rangle) \otimes (|I_z = +1\rangle + |I_z = -1\rangle)$. This superposition precedes because we are not in resonance. After a time $\tau = \frac{\pi}{\Delta}$ we have the state $(|S_z = 0\rangle - |S_z = -_{\theta,B_\parallel}\rangle) \otimes (|I_z = +1\rangle + |I_z = -1\rangle)$. The second $\frac{\pi}{2}$ pulse recovers the initial state $|S_z = 0\rangle \otimes (|I_z = +1\rangle + |I_z = -1\rangle)$. The FID sequence acts as an identity.

We remind that dressed states are sensitive to the magnetic field only at the second order, while the partially dressed states are sensitive to the magnetic field at the first order, being characterized by a nonzero expectation value of the axial spin $\langle S_z\rangle \neq 0$. This paves the way for applications in magnetic field sensing. For this kind of application, working in point A in Fig. 1 is not ideal since the degenerate partially dressed states correspond to two opposite values of $\langle S_z\rangle$, and a magnetic field $B_\parallel^{\text{sense}}$ will cause two opposite detunings [61]. The effect of these detunings will tend to cancel each other in a typical magnetic field measurement.

For these reasons, we apply a small bias magnetic field $B_\parallel = \frac{A_\parallel}{g_e\mu_B} = 0.08$ mT, corresponding to point B of Fig. 1, where there are three resonances, one ν_1, belonging to a dressed state, and two ν_2 and ν_3 belonging to two partially dressed states with two different values of $\langle S_z\rangle$. The results of FID measurement performed under this regime are shown in Figs. 3(b) and 3(c). Figure 3(b) shows a measurement taken on resonance with the $I_z = -1$ state ($\nu_{\text{MW}} = \nu_{B,\text{dres}}$), where a combination of three resonance contributions properly describes the experimental data:

$$\begin{aligned} y_{B1} &= y_{B1,I_z=-1} + y_{B1,I_z=0} + y_{B1,I_z=1}, \\ y_{B1,I_z=-1}(t) &= \frac{1}{2}\left[1 - \frac{A_{B1}}{y_{0,B1}} \frac{\Omega^2}{\Omega^2 + \delta_1^2} \cos\left[\delta_1 t + 2\arcsin\left(\frac{\delta_1}{\Omega}\right)\right] e^{-(\frac{t}{T^*_{2\ \text{dressed},I_z=-1}})^p}\right], \\ y_{B1,I_z=0}(t) &= \frac{1}{2}\left[1 - \frac{A_{B1}}{y_{0,B1}} \frac{\Omega^2}{\Omega^2 + \Delta_{1,B1,\text{FID}}^2} \cos\left[\Delta_{1,B1,\text{FID}} t + 2\arcsin\left(\frac{\Delta_{1,B1,\text{FID}}}{\Omega}\right)\right] e^{-(\frac{t}{T^*_{2\ \text{part-dressed-2},I_z=0}})^p}\right], \\ y_{B1,I_z=1}(t) &= \frac{1}{2}\left[1 - \frac{A_{B1}}{y_{0,B1}} \frac{\Omega^2}{\Omega^2 + \Delta_{3,B1,\text{FID}}^2} \cos\left[\Delta_{3,B1,\text{FID}} t + 2\arcsin\left(\frac{\Delta_{3,B1,\text{FID}}}{\Omega}\right)\right] e^{-(\frac{t}{T^*_{2\ \text{part-dressed-3},I_z=1}})^p}\right] \end{aligned} \tag{14}$$

The first component is a very slow oscillating exponential, associated with the on-resonance dressed state with $I_z = -1$. This slow oscillation of frequency $\delta_1 = 81$ kHz is due to nonoptimal experimental conditions. Then, there are two faster-oscillating exponentials corresponding to detunings $\Delta_{1,B1,\text{FID}} = \nu_{B,\text{dres}} - \nu_{B,\text{p-dres2}}$ and $\Delta_{3,B1,\text{FID}} = \nu_{B,\text{dres}} -$

$\nu_{B,\text{p-dres3}}$, which belong to two partially dressed states. The different components exhibit different T_2^* values. Similarly to point A, the dressed states exhibit a longer T_2^* than partially dressed states. Moreover, T_2^* decreases moving from partially dressed state 2 to partially dressed state 3 because of an associated increase in $\langle S_z \rangle$ (see Table I).

A similar behavior in T_2^* is observed when FID measurements are performed on resonance with the partially dressed state having $I_z = 0$ ($\nu_{\text{MW}} = \nu_{B,\text{p-dres2}}$) [see Fig. 3(c)]. In this case, the three components describing the experimental data are

$$\begin{aligned}
y_{B2} &= y_{B2,I_z=-1} + y_{B2,I_z=0} + y_{B2,I_z=1},\\
y_{B2,I_z=-1}(t) &= \frac{1}{2}\left[1 - \frac{A_{B2}}{y_{0,B2}}\frac{\Omega^2}{\Omega^2+\Delta^2_{1,B2,\text{FID}}}\cos\left[\Delta_{1,B2,\text{FID}}t + 2\arcsin\left(\frac{\Delta_{1,B2,\text{FID}}}{\Omega}\right)\right]e^{-(\frac{t}{T^*_{2\ \text{dressed},I_z=-1}})^p}\right],\\
y_{B2,I_z=0}(t) &= \frac{1}{2}\left[1 - \frac{A_{B2}}{y_{0,B2}}\frac{\Omega^2}{\Omega^2+\delta_2^2}\cos\left[\delta_2 t + 2\arcsin\left(\frac{\delta_2}{\Omega}\right)\right]e^{-(\frac{t}{T^*_{2\ \text{part-dressed-2},I_z=0}})^p}\right],\\
y_{B2,I_z=1}(t) &= \frac{1}{2}\left[1 - \frac{A_{B2}}{y_{0,B2}}\frac{\Omega^2}{\Omega^2+\Delta^2_{2,B2,\text{FID}}}\cos\left[\Delta_{2,B2,\text{FID}}t + 2\arcsin\left(\frac{\Delta_{2,B2,\text{FID}}}{\Omega}\right)\right]e^{-(\frac{t}{T^*_{2\ \text{part-dressed-3},I_z=1}})^p}\right].
\end{aligned} \tag{15}$$

There is one very slow oscillating exponential associated with the on-resonance partially dressed state $I_z = 0$, at a frequency $\delta_2 = 156$ kHz. Again, this slow oscillation is due to nonoptimal experimental conditions. Then there are two faster-oscillating exponentials corresponding to the detunings $\Delta_{1,B2,\text{FID}} = \nu_{B,\text{p-dres2}} - \nu_{B,\text{dres}}$ and $\Delta_{2,B2,\text{FID}} = \nu_{B,\text{p-dres2}} - \nu_{B,\text{p-dres3}}$. Under these experimental conditions as well, the value of T_2^* depends on the degree to which a state is dressed and not on the value of the driving microwave frequency ν_{MW}. The detunings $\Delta_{1,B1,\text{FID}}$, $\Delta_{1,B2,\text{FID}}$ are quite close to each other and are compatible with $\Delta_{1,\text{cw}}$. The detunings $\Delta_{3,B1,\text{FID}}$ and $\Delta_{2,B2,\text{FID}}$ are compatible, respectively, with $\Delta_{3,\text{cw}}$ and $\Delta_{2,\text{cw}}$ (see Supplemental Material [44]). The contrast coefficients A_{B1} and A_{B2} are compatible. As in point A, we decided to use the same contrast coefficient and Rabi frequency for dressed and partially dressed states. This means that we consider negligible the difference in the driving strength due to the polarizations.

We suggest that a sensing regime working in point B in Fig. 1 represents an interesting alternative to current methods [17–19,21] to perform magnetic measurements decoupled from temperature effects. We consider both continuous-wave (CW) and pulsed measurements methods. In CW measurements, if the two resonances can be resolved, we can use the four-point method: i.e., we choose two symmetric points f_1 and f_2 on the resonance of the dressed state, and two symmetric points f_3 and f_4 on the resonance of the partially dressed state. The difference in photoluminesce Δ_{PL} on the dressed peak will depend only temperature variation Δ_T:

$$X1 = \Delta_{\text{PL}}(f_2) - \Delta_{\text{PL}}(f_1) \propto k_T \Delta_T. \tag{16}$$

The difference in photoluminescence on the partially dressed peak will depend on temperature variation Δ_T and on axial magnetic field variation $\Delta_{B_\parallel}$:

$$Y1 = \Delta_{\text{PL}}(f_2) - \Delta_{\text{PL}}(f_1) \propto k_T \Delta_T + c g \mu_B \Delta_{B_\parallel}, \tag{17}$$

where c depends on how much the partially dressed state is sensitive to the magnetic field, as detailed below. The difference

$$Y1 - X1 \propto c g_e \mu_B \Delta_{B_\parallel} \tag{18}$$

depends only on the variation of the axial magnetic field.

Now, let us compare the sensitivity of this measurement with respect to the one of the strong-axial-field measurement using an analogous four-points method. Generally, the states involved in the four-point measurements method are the typical strong-axial-field states $|S_z = +1\rangle$ and $|S_z = -1\rangle$. The sensitivity expression for a continuous-wave measurement is

$$\eta_{\text{cw}} \propto \frac{h}{g_e \mu_B} \frac{\Delta\nu}{C_{\text{cw}}\sqrt{R}}, \tag{19}$$

where $\Delta\nu$ is the resonance linewidth, C_{cw} is the cw contrast, and R is the photon detection rate [22]. We compare the cw-odmr spectrum for dressed ($I_z = -1$) and partially dressed state ($I_z = 0$) in Fig. 3(a) with the strong-axial-field spectrum of NV$_2$ family in Fig. 6. Let us start considering also for the strong-axial-field scenario a single hyperfine level. We have to take into account the following effects: (i) the decrease in $\Delta\nu$ for dressed and partially dressed states compared to strong-axial-field states, (ii) how much the eigenergy of the partially dressed state is sensitive to a variation of axial magnetic field, i.e., the factor c in Eqs. (17) and (18), and (iii) the increase in the CW contrast due to higher mw power in strong-axial-field states. The linewidth enters as a factor

$$l = \frac{w_{B,I_z=-1} + w_{B,I_z=0}}{2} \frac{1}{w_{\text{saf}}} = 0.25. \tag{20}$$

The factor c that quantifies the dependence of the eigenergy of the partial dressed is related to the derivative of the curve in Fig. 1(d) at $B_\parallel = A_\parallel / g_e \mu_B$. An analytical expression of c can be derived from Eq. (9):

$$\begin{aligned}
c =& \frac{1}{g\mu_B} \frac{dE^{(2)}_{+,\theta,\mathcal{B}_\parallel}}{dB_\parallel}\Big|_{B_\parallel = A_\parallel/g_e\mu_B} - \frac{dE^{(2)}_0}{dB_\parallel}\\
=& \frac{1}{(1 + E_{\text{gap}}/2A_\parallel)^{\frac{1}{2}}}.
\end{aligned} \tag{21}$$

That is $c = 0.81$ for the parameters considered. The increase in contrast $r = R$:

$$r = \frac{R_{B,I_z=-1} + R_{B,I_z=0}}{2}\frac{1}{R_{\mathrm{saf}}} = 0.41. \tag{22}$$

Taking into account both effects, we have an improvement of a factor $z = \frac{\eta_{pd}}{\eta_{\mathrm{saf}}} = \frac{l}{c * r} = 0.75$ in the sensitivity. Hence, considering a single hyperfine resonance, there is a small advantage in magnetic sensitivity. But it has to be considered that in a strong-axial-field magnetometry measurement (i) all the hyperfine resonances relative to the same strong-axial-field state will be driven simultaneously, leading to an improvement of the contrast by a factor of 2 [62], (ii) both strong-axial-field states are magnetically sensitive leading to an improvement in sensitivity of a further factor 2. Hence, the strong-axial-field configuration is advantageous in terms of magnetic sensitivity by a factor 4. Despite the advantage in sensitivity of the strong-axial-field configuration, our proposal still presents an advantage from an experimental point of view. The dressed and partially dressed states are, at working point B, closer in frequency compared to the states in strong-axial-field configuration allowing the simultaneous interrogation of dressed and partially dressed states using an MW local oscillator mixed with a tunable RF source. Regarding pulsed techniques, the idea is to create a superposition of nuclear states, and then apply a sequence of rectangular pulses that excite both resonances, similar to the ones used for quantum beats magnetometry. In detail, the method will consist of the following steps:

(1) Initialization in the state $|S_z = 0\rangle(|I_z = 0\rangle + |I_z = -1\rangle)$.

(2) Application of a nonselective electronic π pulse in order to create the superposition $|S_z = +\rangle|I_z = +1\rangle + |S_z = \text{p-dres2}\rangle|I_z = 0\rangle$.

(3) Free evolution for a time τ. The state vector at the end of the evolution will be $|S_z = +\rangle|I_z = +1\rangle e^{\nu_{B,\mathrm{dres}}\tau} + |S_z = \text{p-dres2}\rangle|I_z = 0\rangle e^{\nu_{B,\text{p-dres2}}\tau}$.

(4) Application of a selective π, i.e., a $\mathrm{C}_n\mathrm{NOT}_e$ to convert the difference in phase to a difference in population.

(5) Readout of the population.

The key point is that the phase difference, and hence the population difference, will depend only on the difference $\nu_{B,\mathrm{dres}} - \nu_{B,\text{p-dres2}}$, which depends only on the variation $\Delta_{B_\parallel}$ of the axial field.

Generally, with quantum beats magnetometry, the states being simultaneously affected are the typical strong-axial-field states $|S_z = +1\rangle$ and $|S_z = -1\rangle$, while in this case, the dressed and partially dressed states would be used. The primary advantage of our proposal is that the dressed and partially dressed states are, at working point B, closer in frequency compared to the $|S_z = +1\rangle$ and $|S_z = -1\rangle$ states in strong-axial-field configuration. This allows for lower power pulses, providing an advantage, for instance, in sensing biological systems.

It is difficult to quantify the possible improvement in sensitivity of this experiment compared to strong-axial-field configuration. The appropriate expression of sensitivity is the one for Ramsey measurements for double quantum magnetometry [22]:

$$\eta_{\mathrm{Ramsey}} \propto \frac{\hbar}{\Delta m_s g_e \mu_B}\frac{1}{C_{\mathrm{FID}}^{-(\frac{\tau}{T_2,DQ^*})^p}\sqrt{N}}\frac{\sqrt{t_i + \tau + t_R}}{\tau}, \tag{23}$$

where Δm_s is the difference in spin quantum number between the two interferometry states, C_{FID} is the FID contrast, t_i is the initialization time, τ is the measurement time, t_R is the read-out time, T_2, DQ^* is the coherence time in a double magnetometry experiment. The measured coherence times presented in this paper are all single quantum coherence times. Double quantum coherence times are generally quite different because they are not sensitive to common mode source of decoherence [22]. The experimental realization of the proposed protocol and the study of its sensitivity are the objects for future investigations.

IV. CONCLUSIONS

Free induction decay (FID) measurements have been carried on in the presence of a weak orthogonal field and a total electric field for an ensemble of nitrogen vacancy centers. First, the competition between the weak orthogonal field and the total electric field was considered, showing that the resulting eigenstates are dressed states, balanced superposition of strong-axial-field states, rotated in the orthogonal plane. The explicit formula for the rotation angle was obtained from the expression of the exact eigenstates (up to now in literature only calculations in the perturbative approach were available). Then, the role of axial magnetic fields in creating unbalanced superposition of strong-axial-field states, which we call partially dressed states, was described. Two working points were studied experimentally: one with a null axial magnetic field applied and a second with an axial magnetic field matching the hyperfine field caused by the ^{14}N nucleus. In both working points, we observed the presence of dressed and partially dressed states in the FID measurements. Dressed and partially dressed states can be distinguished by different coherence time T_2^*, which shows a decrease when transitioning from dressed to partially dressed states. Compared to the widely studied strong-axial-field states, the coherence time T_2^* is enhanced in dressed and partially dressed states. The possibility to simultaneously drive dressed and partially dressed states using a single microwave opens up interesting applications in quantum computation and quantum sensing, see, e.g., Ref. [60] where a repetitive readout protocol on NV ensemble is exploited. We can use the findings of this paper for the selective magnetic field sensing part and the $\mathrm{C}_n\mathrm{NOT}_e$ previously described to write the state on the N nucleus.

ACKNOWLEDGMENTS

E.B. thanks A. Rigamonti for helpful discussions. This research has been carried on in the context of Project 23NRM04 NoQTeS (European Partnership on Metrology project, co-financed from the European Union's Horizon Europe Research and Innovation Programme and by the Participating States). Project Qutenoise (call Trapezio of San Paolo Foundation). Experiment QUISS funded by INFN

CSN5. Project Promise funded by the European Union's Horizon Europe under the Grant Agreement No. 101189611. This research has also been funded by the Italian Ministry of University and Research (MUR), "NEXT- GENERATION METROLOGY", FOE 2023 (Ministry Decree n. 789/2023). Z.P. wish to acknowledge the National Collaborative Research Infrastructure Strategy (NCRIS) funding provided by the Australian Government for this research. J.F. acknowledges support from MUR Project PE_00000023 -NQSTI - SPOKE 4- CUP B53C22004170006. The authors also wish to thank F. Saccomandi for the technical support in developing the magnetic field control system.

DATA AVAILABILITY

The data that support the findings of this article are not publicly available upon publication because it is not technically feasible and/or the cost of preparing, depositing, and hosting the data would be prohibitive within the terms of this research project. The data are available from the authors upon reasonable request.

APPENDIX A: COMPETITION BETWEEN ORTHOGONAL TOTAL ELECTRIC FIELD AND ORTHOGONAL MAGNETIC FIELD (EXACT SOLUTION)

1. Problem setup

We consider the Hamiltonian

$$\mathcal{H}_{\text{elec-orth}} = D_{\text{gs}} S_z^2 - d_\perp\left[\Pi_x\left(S_x^2 - S_y^2\right) - \Pi_y(S_xS_y + S_yS_x)\right] + g_e\mu_B B_x S_x + g_e\mu_B B_y S_y, \tag{A1}$$

where $\vec{B}$ is the magnetic field and $\vec{\Pi} = \vec{E} + \vec{\sigma}$ is the total electric field that encompasses both the effect of the static electric field and of the strain. This Hamiltonian in the basis $|S_z = +1\rangle$, $|S_z = 0\rangle$, $|S_z = -1\rangle$ can be rewritten as

$$H_{\text{elec-orth}} = \begin{pmatrix} D_{\text{gs}} & \frac{\mathcal{B}_\perp[\cos(\phi_B) - i\sin(\phi_B)]}{\sqrt{2}} & -\mathcal{E}[\cos(\phi_\Pi) + i\sin(\phi_\Pi)] \\ \frac{\mathcal{B}_\perp[\cos(\phi_B) + i\sin(\phi_B)]}{\sqrt{2}} & 0 & \frac{\mathcal{B}_\perp[\cos(\phi_B) - i\sin(\phi_B)]}{\sqrt{2}} \\ -\mathcal{E}[\cos(\phi_\Pi) - i\sin(\phi_\Pi)] & \frac{\mathcal{B}_\perp[\cos(\phi_B) + i\sin(\phi_B)]}{\sqrt{2}} & D_{\text{gs}} \end{pmatrix}, \tag{A2}$$

where we used the quantities defined in Eqs. (4) and (5).

2. Computation of eigenvalues

The eigenvalues of the Hamiltonian in Eq. (A1) are obtained by solving

$$\det(H_{\text{elec-orth}} - \lambda\mathbb{I}) = 0 \tag{A3}$$

that leads to a cubic equation in λ. The three exact solutions correspond to the three exact eigenvalues $E_{0,\text{exact}}$, $E_{1,\text{exact}}$, $E_{2,\text{exact}}$. We have rewritten each eigenvalue as a series expansion of $\zeta = \frac{B_\perp}{D_{\text{gs}}} \ll 1$ where we exploited the ancillary parameter $R = \frac{\mathcal{E}}{\frac{\mathcal{B}_\perp^2}{D_{\text{gs}}}} = \frac{\mathcal{E}}{\zeta^2 D_{\text{gs}}}$ to describe the competing effect between $\mathcal{B}_\perp$ and $\mathcal{E}$ in the physics of the NV center. Then, only the terms till the second order in ζ were kept. The resulting approximated eigenvalues are

$$\begin{aligned} E_0 &= -D_{\text{gs}}\zeta^2 = -\frac{\mathcal{B}_\perp^2}{D_{\text{gs}}}, \\ E_1 &= D_{\text{gs}} + \frac{1}{2}D_{\text{gs}}\zeta^2 - \left[R^2 + \frac{1}{4} - R\cos(2\phi_{B_\perp} + \phi_\Pi)\right]^{\frac{1}{2}} D_{\text{gs}}\zeta^2 = D_{\text{gs}} + \frac{\mathcal{B}_\perp^2}{2D_{\text{gs}}} - \left[\left(\frac{\mathcal{B}_\perp^2}{2D_{\text{gs}}}\right)^2 + \mathcal{E}^2 - \mathcal{E}\frac{\mathcal{B}_\perp^2}{D_{\text{gs}}}\cos(2\phi_{B_\perp} + \phi_\Pi)\right]^{\frac{1}{2}}, \\ E_2 &= D_{\text{gs}} + \frac{1}{2}D_{\text{gs}}\zeta^2 + \left[R^2 + \frac{1}{4} - R\cos(2\phi_{B_\perp} + \phi_\Pi)\right]^{\frac{1}{2}} D_{\text{gs}}\zeta^2 = D_{gs} + \frac{\mathcal{B}_\perp^2}{2D_{\text{gs}}} + \left[\left(\frac{\mathcal{B}_\perp^2}{2D_{\text{gs}}}\right)^2 + \mathcal{E}^2 - \mathcal{E}\frac{\mathcal{B}_\perp^2}{D_{\text{gs}}}\cos(2\phi_{B_\perp} + \phi_\Pi)\right]^{\frac{1}{2}}. \end{aligned} \tag{A4}$$

These eigenvalues are the same as the one presented in Ref. [13], a part a factor $\frac{1}{2}$ in first eigenvalue E_0.

We underline that the parameter R quantifies the relative strength of $\mathcal{B}_\perp$ and $\mathcal{E}$. The choice of R expression was inspired by the fact that the term out of diagonal, like $\mathcal{B}_\perp$, appears at second order in standard perturbation theory.

3. Computation of eigenstates

Starting from the exact eigenvalues of energy, obtained by solving Eq. (A3), we obtained the exact eigenvectors. Here we present their first order in ζ:

$$\begin{aligned}
|0\rangle &= \left(\frac{\mathcal{B}_\perp}{D_{\rm gs}}, -\sqrt{2}e^{i\phi_{B_\perp}}, e^{i2\phi_{B_\perp}}\frac{\mathcal{B}_\perp}{D_{\rm gs}}\right),\\
|1\rangle &= \left[1, \frac{1}{\sqrt{2}}e^{i\phi_{B_\perp}}\left(1-\frac{1-2\,\mathrm{R}e^{i(2\phi_{B_\perp}+\phi_\Pi)}}{|1-2\,\mathrm{R}e^{i(2\phi_{B_\perp}+\phi_\Pi)}|^2}\right)\frac{\mathcal{B}_\perp}{D_{\rm gs}}, -e^{i2\phi_{B_\perp}}\frac{1-2\,\mathrm{R}e^{-i(2\phi_{B_\perp}+\phi_\Pi)}}{|1-2\,\mathrm{R}e^{-i(2\phi_{B_\perp}+\phi_\Pi)}|^2}\right],\\
|2\rangle &= \left[1, \frac{1}{\sqrt{2}}e^{i\phi_{B_\perp}}\left(1+\frac{1-2\,\mathrm{R}e^{i(2\phi_{B_\perp}+\phi_\Pi)}}{|1-2\,\mathrm{R}e^{i(2\phi_{B_\perp}+\phi_\Pi)}|^2}\right)\frac{\mathcal{B}_\perp}{D_{\rm gs}}, e^{i2\phi_{B_\perp}}\frac{1-2\,\mathrm{R}e^{-i(2\phi_{B_\perp}+\phi_\Pi)}}{|1-2\mathrm{R}e^{-i(2\phi_{B_\perp}+\phi_\Pi)}|^2}\right].
\end{aligned} \tag{A5}$$

It is interesting to discuss the limit case $R \ll 1$, i.e., when $\mathcal{B}_\perp$ is predominant. In this case, the eigenstates are, after collecting a global phase factor $e^{i\phi_{B_\perp}}$,

$$\begin{aligned}
|0\rangle &= \left(e^{-i\phi_{B_\perp}}\frac{\mathcal{B}_\perp}{D_{gs}}, -\sqrt{2}, e^{i\phi_{B_\perp}}\frac{\mathcal{B}_\perp}{D_{gs}}\right) = -\sqrt{2}\left(|S_z=0\rangle - \frac{\mathcal{B}_\perp}{D_{\rm gs}}|+\rangle_{\phi_{B_\perp}}\right),\\
|1\rangle &= (e^{-i\phi_{B_\perp}}, 0, -e^{i\phi_{B_\perp}}) = \sqrt{2}|-\rangle_{\phi_{B_\perp}},\\
|2\rangle &= \left(e^{-i\phi_{B_\perp}}, \sqrt{2}\frac{\mathcal{B}_\perp}{D_{\rm gs}}, +e^{i\phi_{B_\perp}}\right) = \sqrt{2}\left(|+\rangle_{\phi_{B_\perp}} + \frac{\mathcal{B}_\perp}{D_{\rm gs}}|S_z=0\rangle\right),
\end{aligned} \tag{A6}$$

where we introduced the vectors

$$\begin{aligned}
|-\rangle_{\phi_{B_\perp}} &= \frac{1}{\sqrt{2}}(e^{-i\phi_{B_\perp}}, 0, -e^{i\phi_{B_\perp}}) = \frac{1}{\sqrt{2}}(e^{-i\phi_{B_\perp}}|S_z=+1\rangle - e^{i\phi_{B_\perp}}|S_z=-1\rangle),\\
|+\rangle_{\phi_{B_\perp}} &= \frac{1}{\sqrt{2}}(e^{-i\phi_{B_\perp}}, 0, +e^{i\phi_{B_\perp}}) = \frac{1}{\sqrt{2}}(e^{-i\phi_{B_\perp}}|S_z=+1\rangle + e^{i\phi_{B_\perp}}|S_z=-1\rangle).
\end{aligned} \tag{A7}$$

Considering Eqs. (A6), it is clear that for $R \ll 1$ the effect of the orthogonal magnetic field is

(i) to rotate the original dressed states $|-\rangle$ and $|+\rangle$ of angle $\phi_{B_\perp}$ equal to field orientation and

(ii) create a small mixing between $|+\rangle_{\phi_{B_\perp}}$ and $|S_z=0\rangle$ state.

These results are usually derived using second-order degenerate perturbation theory. Now, let us turn our attention to the general case $R \neq 0$. If we introduce the angle

$$\theta = \frac{1}{2}\arg\left(e^{i2\phi_{B_\perp}}\frac{1-2\,\mathrm{R}e^{-i(2\phi_{B_\perp}+\phi_\Pi)}}{|1-2\,\mathrm{R}e^{-i(2\phi_{B_\perp}+\phi_\Pi)}|^2}\right) = \frac{1}{2}\arg(e^{2i\phi_{B_\perp}} - 2\,\mathrm{R}e^{-i\phi_\Pi}) \tag{A8}$$

and we collect a phase factor $e^{i\theta}$ in Eqs. (A5) we obtain

$$\begin{aligned}
|0\rangle &= -\sqrt{2}e^{i(\phi_{B_\perp}-\theta)}\left[|S_z=0\rangle - \frac{\mathcal{B}_\perp}{D_{\rm gs}}[\cos(\phi_{B_\perp}-\theta)|+\rangle_\theta + i\sin(\phi_{B_\perp}-\theta)|-\rangle_\theta]\right],\\
|1\rangle &= \sqrt{2}\left(|-\rangle_\theta + \frac{\mathcal{B}_\perp}{D_{\rm gs}}i\sin(\phi_{B_\perp}-\theta)|S_z=0\rangle\right),\\
|2\rangle &= \sqrt{2}\left(|+\rangle_\theta + \frac{\mathcal{B}_\perp}{D_{\rm gs}}\cos(\phi_{B_\perp}-\theta)|S_z=0\rangle\right).
\end{aligned} \tag{A9}$$

Equation (A9) tells us that the effect of orthogonal magnetic and electric field is to rotate the original dressed states $|-\rangle$ and $|+\rangle$ of an angle θ. Thus, we can rename the eigenergies as

$$E_{-,\theta} = E_1, \quad E_{+,\theta} = E_2. \tag{A10}$$

The detailed calculations leading to Eqs. (A7) and (A9) can be found in the Supplemental Material [44].

APPENDIX B: EFFECT OF AN AXIAL MAGNETIC FIELD

We have shown in the previous sections that the combined contribution of a total electric field and a weak orthogonal field can be summarized in three effects:

(i) Rotation of the original dressed states $|S_z=0\rangle, |-\rangle, |+\rangle$ of an angle θ along the z axis, giving the eigenstates $|S_z=0\rangle, |-\rangle_\theta, |+\rangle_\theta$. This is valid if we neglegt the small mixing between $|-\rangle_\theta, |+\rangle_\theta$ and $|S_z=0\rangle_\theta$.

(ii) Creation of an energy gap between $|+\rangle_\theta$ and $|-\rangle_\theta$, $E_{\rm gap} = 2[(\frac{\mathcal{B}_\perp^2}{2D_{\rm gs}})^2 + \mathcal{E}^2 - \mathcal{E}\frac{\mathcal{B}_\perp^2}{D_{\rm gs}}\cos(2\phi_{B_\perp})]^{\frac{1}{2}}$.

(iii) Decrease in energy of the $|0\rangle$ state to $E_0 = -\frac{\mathcal{B}_\perp^2}{D_{\rm gs}} < 0$

Considering negligible the mixing between $|-\rangle_\theta$, $|+\rangle_\theta$, and $|S_z = 0\rangle$, we can rewrite the Hamiltonian of the system as

$$H_{B_\parallel = 0} = \begin{pmatrix} E_0 - E_m & 0 & 0 \\ 0 & -\frac{E_{\rm gap}}{2} & 0 \\ 0 & 0 & +\frac{E_{\rm gap}}{2} \end{pmatrix} \tag{B1}$$

in the basis $|0\rangle_\theta, |-\rangle_\theta, |+\rangle_\theta$, where $E_m = \frac{E_{+,\theta} + E_{-,\theta}}{2} = D_{\rm gs} + \frac{\mathcal{B}_\perp^2}{2D_{\rm gs}}$ was chosen as the zero of the energy scale.

Following Ref. [35] if we consider a magnetic field $B_\parallel$ aligned along the NV axis, the total Hamiltonian will be

$$H_{B_\parallel \neq 0} = \begin{pmatrix} E_0 - E_m & & 0 \\ 0 & -\frac{E_{\rm gap}}{2} & \mathcal{B}_\parallel \\ 0 & \mathcal{B}_\parallel & +\frac{E_{\rm gap}}{2} \end{pmatrix}, \tag{B2}$$

where $\mathcal{B}_\parallel = g\mu_B B_\parallel$. If we consider only the subspace $|-\rangle_\theta, |+\rangle_\theta$ the Hamiltonian becomes

$$H_{\rm red} = \begin{pmatrix} -\frac{E_{\rm gap}}{2} & \mathcal{B}_\parallel \\ \mathcal{B}_\parallel & +\frac{E_{\rm gap}}{2} \end{pmatrix}. \tag{B3}$$

If we now change the basis to $(|S_z = -1\rangle_\theta = e^{i\theta}|S_z = -1\rangle$, $|S_z = +1\rangle_\theta = e^{-i\theta}|S_z = -1\rangle$, we have

$$H_{\rm red} = \begin{pmatrix} -\mathcal{B}_\parallel & \frac{E_{\rm gap}}{2} \\ \frac{E_{\rm gap}}{2} & \mathcal{B}_\parallel \end{pmatrix}. \tag{B4}$$

This Hamiltonian can be diagonalized exactly, considering the system as one with effective spin $s = \frac{1}{2}$. The resulting eigenvectors are

$$\begin{aligned} |-\rangle_{\theta,\mathcal{B}_\parallel} &= \sin\left(\frac{\gamma}{2}\right) e^{-i\theta}|S_z = +1\rangle - \cos\left(\frac{\gamma}{2}\right) e^{i\theta}|S_z = -1\rangle, \\ |+\rangle_{\theta,\mathcal{B}_\parallel} &= \cos\left(\frac{\gamma}{2}\right) e^{-i\theta}|S_z = +1\rangle + \sin\left(\frac{\gamma}{2}\right) e^{i\theta}|S_z = -1\rangle \end{aligned} \tag{B5}$$

with

$$\tan\gamma = \frac{E_{\rm gap}/2}{\mathcal{B}_\parallel}. \tag{B6}$$

The corresponding eigenenergies are

$$\begin{aligned} E_{0'}^{(2)} &= -\frac{\mathcal{B}_\perp^2}{D_{\rm gs}}, \\ E_{-,\theta,\mathcal{B}_\parallel}^{(2)} &= E_m - \sqrt{(E_{\rm gap}/2)^2 + \mathcal{B}_\parallel^2} = D_{gs} + \frac{\mathcal{B}_\perp^2}{2D_{gs}} - \sqrt{(E_{\rm gap}/2)^2 + \mathcal{B}_\parallel^2}, \\ E_{+,\theta,\mathcal{B}_\parallel}^{(2)} &= E_m + \sqrt{(E_{\rm gap}/2)^2 + \mathcal{B}_\parallel^2} = D_{\rm gs} + \frac{\mathcal{B}_\perp^2}{2D_{\rm gs}} + \sqrt{(E_{\rm gap}/2)^2 + \mathcal{B}_\parallel^2}. \end{aligned} \tag{B7}$$

We underline that the states $|-\rangle_{\theta,\mathcal{B}_\parallel}$, $|+\rangle_{\theta,\mathcal{B}_\parallel}$ are in general a nonbalanced superposition of high-field states $|S_z = +1\rangle$, $|S_z = +1\rangle$. The dependence of the coefficients of high-field states as function of the axial field is shown in Fig. 4 for the $|+\rangle_{\theta,\mathcal{B}_\parallel}$ where we consider $0 < \gamma < \pi$. For $\mathcal{B}_\parallel = 0$, $\gamma = \frac{\pi}{2}$ the coefficients are equal in modulus. Increasing $\mathcal{B}_\parallel$ to higher positive values, we have that $\gamma < \frac{\pi}{2}$ and the coefficient relative to the state $|S_z = +1\rangle$ becomes larger than the one relative to $|S_z = 1\rangle$. Decreasing $\mathcal{B}_\parallel$ to lower positive values, the coefficient relative to the state $|S_z = -1\rangle$ becomes larger than the one relative to $|S_z = +1\rangle$. This explains the transition from dressed states to partially dressed states and then to quasi-high-field states.

The expectation values of the axial spin are

$$\begin{aligned} {}_{\theta,\mathcal{B}_\parallel}\langle +|S_z|+\rangle_{\theta,\mathcal{B}_\parallel} &= \cos^2\left(\frac{\gamma}{2}\right) - \sin^2\left(\frac{\gamma}{2}\right) = \cos(\gamma), \\ {}_{\theta,\mathcal{B}_\parallel}\langle -|S_z|-\rangle_{\theta,\mathcal{B}_z} &= \sin^2\left(\frac{\gamma}{2}\right) - \cos^2\left(\frac{\gamma}{2}\right) = -\cos(\gamma), \\ \langle 0|S_z|0\rangle_{\mathcal{B}_\parallel} &= 0. \end{aligned} \tag{B8}$$

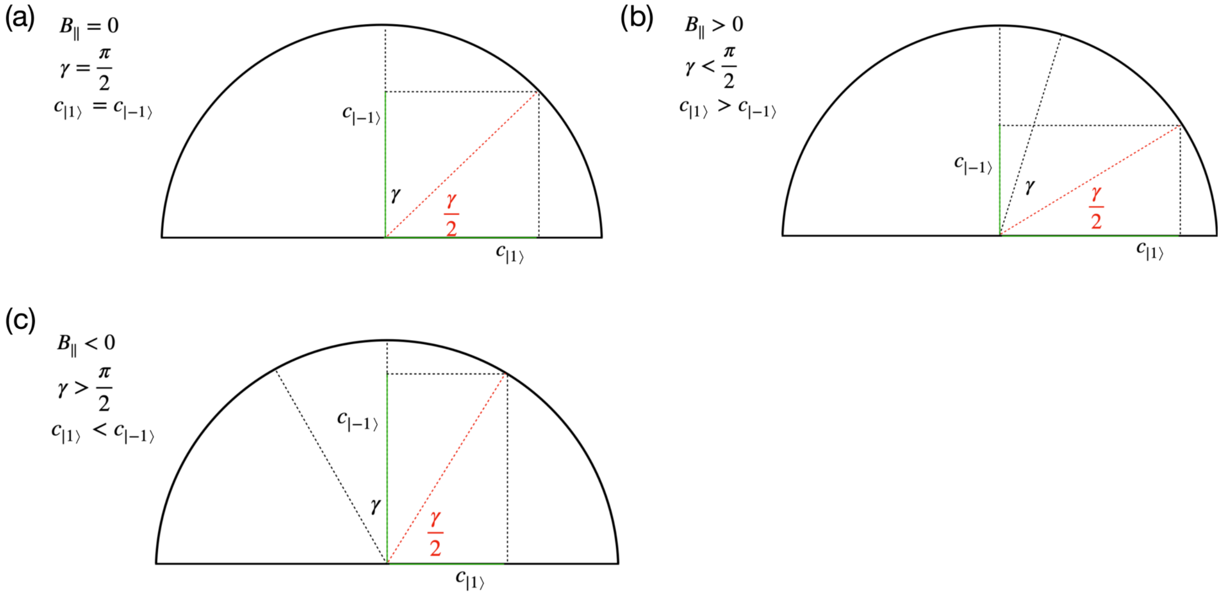

FIG. 4. Different balance of coefficients of high field for (a) $B_\parallel = 0$, (b) $B_\parallel > 0$, (c) $B_\parallel < 0$. For $B_\parallel = 0$ the coefficients are equal, and the superposition is balanced, corresponding to dressed states. For $B_\parallel > 0$ the superposition is unbalanced toward $|S_z = +1\rangle$ and for$B_\parallel < 0$ the superposition is unbalanced toward $|S_z = -1\rangle$.

From this expression it follows that partially dressed states for opposite values of axial field $B_\parallel$ have opposite values of $\langle S_z\rangle$ because $\cos(\frac{\pi}{2} - \gamma) = -\cos(\frac{\pi}{2} - \gamma)$, where, again, we recall that $\gamma = \frac{\pi}{2}$ for $\mathcal{B}_\parallel = 0$.

Let us now consider the mixing between $|-\rangle_\theta$, $|+\rangle_\theta$, and $|S_z = 0\rangle$, that has not been considered so far, since we intend to prove that it is negligible. The basis to be considered is the one formed by the eigenvectors $|0\rangle$, $|1\rangle$, $|2\rangle$ of Eqs. (A9). On this basis the total Hamiltonian is

$$H_{B_z \neq 0} = \begin{pmatrix} E_0 - E_m & -\frac{\mathcal{B}_\parallel \mathcal{B}_\perp}{2D_{\rm gs}} \cos(\phi_{B_\perp} - \theta) & +i\frac{\mathcal{B}_\parallel \mathcal{B}_\perp}{2D_{\rm gs}} \sin(\phi_{B_\perp} - \theta) \\ -\frac{\mathcal{B}_\parallel \mathcal{B}_\perp}{2D_{\rm gs}} \cos(\phi_{B_\perp} - \theta) & -\frac{E_{\rm gap}}{2} & \mathcal{B}_\parallel \\ -i\frac{\mathcal{B}_\parallel \mathcal{B}_\perp}{2D_{\rm gs}} \sin(\phi_{B_\perp} - \theta) & \mathcal{B}_\parallel & +\frac{E_{\rm gap}}{2} \end{pmatrix}. \tag{B9}$$

Considering our experimental conditions, $\frac{\mathcal{B}_\parallel \mathcal{B}_\perp}{2D_{\rm gs}} i \sin(\phi_{B_\perp} - \theta) \ll E_0 - E_m = D_{\rm gs} + \frac{\mathcal{B}_\perp^2}{D_{\rm gs}}$ and we can consider the term $\frac{\mathcal{B}_\parallel \mathcal{B}_\perp}{2D_{\rm gs}}$ as a perturbation of the Hamiltonian in absence of mixing. Without going into detailed calculations, from perturbation theory, we know that the effect of the perturbation is of the order of $\frac{\mathcal{B}_\parallel^2 \mathcal{B}_\perp^2}{D_{\rm gs}^3}$ on the eigenergies and can be neglected; that was our initial assumption.

APPENDIX C: POLARIZATION

This appendix will study how to excite dressed and partially dressed states using an oscillating magnetic field $\vec{B}_{\rm osc}$ with suitable polarization.

1. Dressed states

We consider the effect of an oscillating magnetic field $\vec{B}_{\rm osc}$ in driving the transition between the state $|0\rangle$ and dressed states ($|+\rangle_\theta$, $|-\rangle_\theta$). If the magnetic field is aligned along the direction defined by θ and the corresponding versor $\hat{v}$, its expression is

$$\vec{B}_{\rm osc} = B_\theta \cos(\omega_d t)\hat{v} = B_\theta \cos(\omega_d t)(\cos\theta \hat{x} + \sin\theta \hat{y}), \tag{C1}$$

where B_θ is the amplitude of the field along θ, and ω_d is the angular frequency. The time-dependent Hamiltonian is

$$H_{0,{\rm dressed}} = D_{gs} S_z^2 + 2\Omega_\theta \cos(\omega_d t)(\cos\theta S_x + \sin\theta S_y), \tag{C2}$$

where $2\Omega_\theta = g\mu_B B_\theta$. For simplicity, we have considered only the part due to zero-field splitting D_{gs}. In the interaction description defined by $H_0^{(1)} = \omega_d S_z^2$, we have

$$\begin{aligned}
H_{1;\text{dressed}} &= U_0^{(1)}(t)^\dagger H_{0,\text{dressed}} U_0^{(1)}(t) - iU_0^{(1)}(t)^\dagger \partial_t U_0^{(1)}(t)\\
&= \begin{bmatrix} D_{\text{gs}} - \omega_d & \sqrt{2}\Omega e^{i\omega_d t}\cos(\omega_d t)(\cos\theta - i\sin\theta) & 0\\ \sqrt{2}\Omega e^{-i\omega_d t}\cos(\omega_d t)(\cos\theta + i\sin\theta) & 0 & \sqrt{2}\Omega e^{-i\omega_d t}(\cos\theta - i\sin\theta)\cos(\omega_d t)\\ 0 & \sqrt{2}\Omega e^{i\omega_d t}\cos(\omega_d t)(\cos\theta + i\sin\theta) & D_{\text{gs}} - \omega_d \end{bmatrix}\\
&\approx \begin{bmatrix} D_{\text{gs}} - \omega_d & \frac{1}{\sqrt{2}}\Omega e^{-i\theta} & 0\\ \frac{1}{\sqrt{2}}\Omega e^{+i\theta} & 0 & \frac{1}{\sqrt{2}}\Omega e^{-i\theta}\\ 0 & \frac{1}{\sqrt{2}}\Omega e^{+i\theta} & D_{\text{gs}} - \omega_d \end{bmatrix},
\end{aligned} \tag{C3}$$

where $U_0^{(1)}(t) = \exp(-i\omega_d S_z^2)$, and we applied the rotating-wave approximation, neglecting the fast terms rotating at $2\omega_d t$ in the second row. From the last row, it is clear that when $\vec{B}_{\text{osc}}$ is aligned with θ, it induces transition between $|0\rangle$ and $|+\rangle_\theta$. Analogously, if, in Eq. (C1), $\vec{B}_{\text{osc}}$ is aligned orthogonal to θ, it induce transitions between $|0\rangle$ and $|-\rangle_\theta$.

2. Partially dressed states

Let us assume now an elliptically polarized MW excitation with the major axis aligned along θ:

$$\begin{aligned}
\vec{B}_{\text{osc}} &= B_\theta \cos(\omega_d t)\hat{v} + B_{\theta+\pi/2}\sin(\omega_d t)\hat{w}\\
&= B_\theta \cos(\omega_d t)[\cos\theta\hat{x} + \sin\theta\hat{y}] + B_{\theta+\pi/2}\cos(\omega_d t)[-\sin\theta\hat{x} + \cos\theta\hat{y}],
\end{aligned} \tag{C4}$$

where B_θ is the amplitude of the field along θ, $\hat{v}$ is the versor defined by θ, $B_{\theta+\pi/2}$ is the amplitude of the field along $\theta + \pi/2$, $\hat{w}$ is the versor defined by $\theta + \pi/2$, with $B_\theta > B_{\theta+\pi/2}$. If $B_\theta = B_{\theta+\pi/2}$, the magnetic field is circularly clockwise polarized. The total time-dependent Hamiltonian is

$$H_{0,\text{p-dressed}} = D_{\text{gs}}S_z^2 + 2\Omega_\theta \cos(\omega_d t)(S_x\cos\theta + S_y\sin\theta) + 2\Omega_{\theta+\pi/2}\sin(\omega_d t)[S_x(-\sin\theta) + S_y\cos\theta)], \tag{C5}$$

where $2\Omega_\theta = g\mu_B B_\theta$ and $2\Omega_{\theta+\pi/2} = g\mu_B B_{\theta+\pi/2}$.

Also in this case, we have considered only the part due to zero-field splitting D_{gs}. We move to the interaction description defined by $H_0^{(1)} = \omega_d S_z^2$:

$$\begin{aligned}
H_{1,\text{p-dressed}} &= U_0^{(1)}(t)^\dagger H_{0,\text{p-dressed}} U_0^{(1)}(t) - iU_0^{(1)}(t)^\dagger \partial_t U_0^{(1)}(t)\\
&= \begin{bmatrix} D_{\text{gs}} - \omega_d & \frac{1}{\sqrt{2}}(\Omega_\theta + \Omega_{\theta+\pi/2})e^{-i\theta} & 0\\ \frac{1}{\sqrt{2}}(\Omega_\theta + \Omega_{\theta+\pi/2})e^{+i\theta} & 0 & \frac{1}{\sqrt{2}}(\Omega_\theta - \Omega_{\theta+\pi/2})e^{-i\theta}\\ 0 & \frac{1}{\sqrt{2}}(\Omega_\theta - \Omega_{\theta+\pi/2})e^{+i\theta} & D_{\text{gs}} - \omega_d \end{bmatrix}.
\end{aligned} \tag{C6}$$

From the last row of Eq. (C6), it can be seen that the elliptically polarized MW excitation drive transition between the states $|0\rangle$ and $|+\rangle_{\theta,\mathcal{B}_\parallel}$ in Eq. (B5), if

$$\cos\left(\frac{\gamma}{2}\right) = \frac{1}{\sqrt{2}}\frac{\Omega_\theta + \Omega_{\theta+\pi/2}}{\sqrt{\Omega_\theta^2 + \Omega_{\theta+\pi/2}^2}}, \quad \sin\left(\frac{\gamma}{2}\right) = \frac{1}{\sqrt{2}}\frac{\Omega_\theta - \Omega_{\theta+\pi/2}}{\sqrt{\Omega_\theta^2 + \Omega_{\theta+\pi/2}^2}}. \tag{C7}$$

Increasing $B_\parallel$, the angle γ goes to 0 [see Eq. (B6)], we have $\Omega_\theta = \Omega_{\theta+\pi/2}$ and we recover the well-known results that transition between $|0\rangle$ and strong-axial-field states are driven by circularly polarized oscillating magnetic field [63]. Similarly, it can be shown that when B_{osc} is aligned with the major axis orthogonal to θ it induces transition between $|0\rangle$ and $|-\rangle_{\theta,\mathcal{B}_\parallel}$.

Summarizing, (i) transitions between $|0\rangle$ and dressed states are promoted by the linearly polarized oscillating magnetic field, aligned along θ, i.e., along the direction determined by the competition between orthogonal magnetic field and total orthogonal electric field, or orthogonal to this direction, (ii) transitions between $|0\rangle$ and partially dressed states are promoted by elliptically polarized oscillating magnetic field aligned or orthogonal to θ, and (iii) furthermore, it is well known that transitions between $|0\rangle$ and strong-axial-field states are promoted by circularly polarized oscillating magnetic field [63].

APPENDIX D: DECOHERENCE IN A FREE INDUCTION DECAY MEASUREMENT FOR A SINGLE NV CENTER

We use a derivation similar to the one presented in [35,56–58]. We first consider the case of a single NV, and then discuss how to generalize the discussion to an ensemble of NV's.

The sources of decoherence for a single NV center are
(1) coupling with ^{13}C,
(2) coupling with ^{14}N or ^{15}N,
(3) coupling with other spins,
(4) temporal fluctuations of external fields.

Decoherence due to the bath of surrounding spins, points 1–3 in the previous list, is a pure quantum phenomenon due to the entanglement of the NV center with the surrounding spin bath [57,64]. For a limited class of problems, with so-called "nonbranching" evolution, we can map the original quantum spin bath onto a classical random magnetic field $\vec{B}_{\text{s-dec}}$ [56]. We can consider this field as aligned along the z axis, $\vec{B}_{\text{s-dec}} = B_{\text{s-rand}}\vec{z}$, since the orthogonal part of this field is due to flip-flop terms in the spin-spin coupling that are suppressed by the big zero-field splitting D_{gs}.

The temporal fluctuations of the external fields (point 4 in the previous list) can be described by two other stochastic magnetic $\vec{B}_{\text{t-dec}}$ and total electric fields $\vec{\Pi}_{\text{t-dec}}$. Finally, we consider that the effect of the spin-spin coupling and of the temporal fluctuations adds up, giving a total stochastic magnetic field $\vec{B}_{\text{dec}} = \vec{B}_{\text{s-dec}} + \vec{B}_{\text{t-dec}}$.

For simplicity, we consider $\vec{B}_{\text{dec}}$ and $\vec{\Pi}_{\text{dec}}$ to have a Gaussian distribution with zero mean and standard deviation $\sigma_{B_{\text{dec},i}}$ and $\sigma_{\Pi_{\text{dec},i}}$ in each Cartesian direction i.

The fluctuations of the stochastic fields $\vec{B}_{\text{dec}}$ and $\vec{\Pi}_{\text{dec}}$ represented by the random variable $\delta\vec{B}_{\text{dec}}$ and $\delta\vec{\Pi}_{\text{dec}}$ induce fluctuations in the eigenenergies of the NV center and consequently fluctuations $\delta\nu$ in the ODMR transition frequencies. Fluctuations $\delta\nu$ in the ODMR transition frequencies will induce a decay in FID signal [35]. To fix the idea let us focus on the $|0\rangle \rightarrow |+\rangle_{\theta,\mathcal{B}_\parallel}$ ODMR transition. In general, the FID signal is proportional to the probability $p_{|0\rangle}$ to be in $|0\rangle$:

$$p_{|0\rangle}(\tau) = \frac{[1-\cos(\phi+\delta\phi)]}{2}, \tag{D1}$$

where τ is the duration of the free precession interval, $\delta\phi = \int_0^\tau 2\pi\,\delta\nu\,dt$ and $\phi = 2\pi\Delta\tau$ are, respectively, the stochastic and static phases acquired during the free precession interval, and $\Delta = \nu_{\text{MW}} - \nu_{+,\theta,\mathcal{B}_\parallel}$ is the detuning between the microwave excitation frequency ν_{MW} and the ODMR transition. If we now consider the average on the different experimental realizations

$$p_{\text{FID}}(\tau) = \langle p_{|0\rangle}(\tau)\rangle = \frac{\left[1-e^{\langle\delta\phi^2\rangle/2}\cos(2\pi\Delta\tau)\right]}{2} \tag{D2}$$

we see that the FID decay is determined by the variance of the stochastic phase acquired during the free precession interval $\langle\delta\phi^2\rangle$, where

$$\langle\delta\phi^2\rangle = 4\pi^2\int_0^\tau dt\int_0^\tau dt'\langle\delta\nu(t)\delta\nu(t')\rangle \tag{D3}$$

and $\langle\delta\nu(t)\delta\nu(t')\rangle$ is the correlation function. To evaluate $\langle\delta\nu(t)\delta\nu(t')\rangle$ we consider the following:

(1) $\delta\vec{B}_{\text{dec}}$ and $\delta\vec{\Pi}_{\text{dec}}$ random variables with correlations functions decaying exponentially,

$$\begin{aligned}\langle\delta B_{\text{dec},i}(t)\delta B_{\text{dec},i}(t')_i\rangle &= \sigma^2_{B_{\text{dec},i}}e^{|t-t'|/\tau_{c,B_{\text{dec},i}}},\\ \langle\delta\Pi_{\text{dec},i}(t)\delta\Pi_{\text{dec},i}(t')_i\rangle &= \sigma^2_{\Pi_{\text{dec},i}}e^{|t-t'|/\tau_{c,\Pi_{\text{dec},i}}},\end{aligned} \tag{D4}$$

where $\delta B_{\text{dec},i}$ and $\delta\Pi_{\text{dec},i}$ are the component of fluctuations of $\vec{B}_{\text{dec}}$ and $\vec{\Pi}_{\text{dec}}$ along the i direction, with $i = x, y, z$.

(2) $\delta\nu_{\text{res}}$ dependence on $\delta B_{\text{dec},i}$ and $\delta\Pi_{\text{dec},i}$ is set by the value of the static fields $\vec{B}$ and $\vec{\Pi}$. Considering $\sigma_{B_{\text{dec},i}} = \sqrt{\langle\delta B^2_{\text{dec},i}\rangle} \ll B_i$ and $\sigma_{\Pi_{\text{dec},i}} = \sqrt{\langle\delta\Pi^2_{\text{dec},i}\rangle} \ll \Pi_i$, $\forall\, i$, δB_{dec} and $\delta\Pi_{\text{dec}}$ act as perturbations on the eigenstates and eigenvalues set by $\vec{B}$ and $\vec{\Pi}$ in the Hamiltonian in Eq. (B2).

Now we will study the different scenarios set by the values of the static fields $\vec{B}$ and $\vec{\Pi}$.

1. Limit case: Weak axial field

To simplify the discussion, let us consider the quantities introduced before:

$$\mathcal{B}_\perp = \frac{g_e\mu_B}{h}B_\perp, \quad \mathcal{E} = d_\perp\Pi_\perp, \quad \mathcal{B}_\parallel = \frac{g_e\mu_B}{h}B_\parallel. \tag{D5}$$

When the condition

$$\sqrt{\mathcal{E}^2 + \frac{\mathcal{B}_\perp^2}{D_{gs}}} \gg \mathcal{B}_\parallel \tag{D6}$$

is satisfied, the eigenstates are dressed states $|0\rangle, |+\rangle_\theta, |-\rangle_\theta$ [see Eqs. (6)]. The eigenenergies are $E_0, E_{+,\theta}, E_{-,\theta}$ [see Eqs. (A4) and (A10)], with

$$E_{\text{gap}} = E_{+,\theta} - E_{-,\theta} = 2\left[\left(\frac{\mathcal{B}_\perp^2}{2D_{\text{gs}}}\right)^2 + \mathcal{E}^2 - \mathcal{E}\frac{\mathcal{B}_\perp^2}{D_{\text{gs}}}\cos(2\phi)\right]^{\frac{1}{2}}. \tag{D7}$$

For a given θ, the angle $\phi = -2\theta + \pi/2$ defines a preferred direction x' for a fluctuation of the total electric field $\delta\Pi_{\text{dec},x'}$. Along this direction, the contribution of the fluctuations of the total electric field $\delta\Pi_{\text{dec},x'}$ enters at first order in the perturbation. Hence, the fluctuations $\delta B_{\text{dec},i}$ and $\delta\Pi_{\text{dec},i}$ induce the following fluctuations in the eigenenergies, considering until the second order:

$$\begin{aligned}\delta E_{+,\theta} =& -d_\perp\delta\Pi_{\text{dec},x'} + \frac{(g_e\mu_B\delta B_{\text{dec},z})^2}{E_{\text{gap}}} + \frac{(d_\perp\delta\Pi_{\text{dec},y'})^2}{E_{\text{gap}}}\\ &+ \frac{(g_e\mu_B\delta B_{\text{dec},x'})^2}{D_{\text{gs}}},\\ \delta E_{-,\theta} =& +d_\perp\delta\Pi_{\text{dec},x'} + \frac{(g_e\mu_B\delta B_{\text{dec},z})^2}{E_{\text{gap}}} + \frac{(d_\perp\delta\Pi_{\text{dec},x'})^2}{E_{\text{gap}}}\\ &+ \frac{(g_e\mu_B\delta B_{\text{dec},y'})^2}{D_{\text{gs}}},\\ \delta E_0 =& -\frac{(g_e\mu_B\delta B_{\text{dec},x'})^2}{D_{\text{gs}}} - \frac{(g_e\mu_B\delta B_{\text{dec},y'})^2}{D_{\text{gs}}},\end{aligned} \tag{D8}$$

where y' is the direction orthogonal to x'. Considering the $|0\rangle \rightarrow |-\rangle_\theta$ ODMR transition, we have the following expression for the fluctuation of the resonance frequency:

$$\delta\nu_+ = \delta E_{+,\theta} - \delta E_0 = -d_\perp \delta\Pi_{\mathrm{dec},x'} + \frac{(g_e\mu_B\delta B_{\mathrm{dec},z})^2}{E_{\mathrm{gap}}}, \tag{D9}$$

where we neglected the term proportional to $\delta B_{\mathrm{dec},x'}$ because $D_{\mathrm{gs}} \gg g\mu_B\delta B_{\mathrm{dec},x'}$, and we neglected the term proportional to $\delta\Pi_{\mathrm{dec},y'}$ because we consider $\vec{\Pi}_{\mathrm{dec}}$ isotropic.

We underline that the effect of fluctuations of the axial magnetic field δB_z is only at the second order, and it is scaled by the value of the energy gap E_{gap}. This is because $|-\rangle_\theta$ is a dressed state with $\langle S_z\rangle = 0$.

If we now consider a slowly fluctuating bath with $\tau \ll \tau_{c,B_{\mathrm{dec},z}}, \tau_{c,\Pi_{dec,y}}$, using the expression in Eqs. (D9) through (D4) and (D3), we can calculate the resulting variance of the phase fluctuation as

$$\langle\delta\phi^2\rangle = 4\pi^2\left[d_\perp^2\sigma^2_{\Pi_{\mathrm{dec},x'}} + \frac{(g_e\mu_B)^4\sigma^4_{B_{\mathrm{dec},z}}}{E^2_{\mathrm{gap}}}\right]\tau^2 \tag{D10}$$

and so, from Eq. (D2), the FID decay

$$p_{\mathrm{FID}}(\tau) = \langle p_{|0\rangle(\tau)}\rangle = \frac{\left[1 - e^{-\left(\frac{\tau}{T_2^*}\right)^2}\cos(2\pi\Delta\tau)\right]}{2}, \tag{D11}$$

with

$$T^*_{2,\mathrm{dressed}} = \frac{1}{\sqrt{2}\pi}\frac{1}{\sqrt{d_\perp^2\sigma^2_{\Pi_{\mathrm{dec},x'}} + \frac{(g_e\mu_B)^4\sigma^4_{B_{\mathrm{dec},z}}}{E^2_{\mathrm{gap}}}}}, \tag{D12}$$

T_2^* defines the characteristic timescale of the FID decay. In this scenario, the more effective decoherence source is $\Pi_{\mathrm{dec},x'}$, i.e., the temporal fluctuations of the electrical fields or of the strain along y' (the direction defined by $\phi = -2\theta + \pi/2$).

2. Limit case: Strong axial field

If we now consider the opposite condition, i.e.,

$$\mathcal{B}_z \gg \sqrt{\mathcal{E}^2 + \frac{\mathcal{B}_\perp^2}{D_{\mathrm{gs}}}} \tag{D13}$$

the eigenstates in this case are strong-axial-field states $|0\rangle, |S_z = +1\rangle, |S_z = -1\rangle$ with corresponding eigenenergies E_0, $E_{-1} = D_{gs} - g_e\mu_B B_z$, $E_{+1} = D_{gs} + g_e\mu_B B_z$. The fluctuations $\delta\vec{B}_{\mathrm{dec}}$ and $\delta\vec{\Pi}_{\mathrm{dec}}$ induce the fluctuations in the eigenergies (until the second order):

$$\begin{aligned}
\delta E_{+1} ={}& g_e\mu_B\delta B_{\mathrm{dec},z} + \frac{d_\perp^2\left(\delta\Pi^2_{\mathrm{dec},x'} + \delta\Pi^2_{\mathrm{dec},y'}\right)}{2g_e\mu_B B_z}\\
&+ \frac{1}{\sqrt{2}}\frac{(g_e\mu_B\delta B_{\mathrm{dec},x'})^2}{D_{\mathrm{gs}} + g_e\mu_B B_z} + \frac{1}{\sqrt{2}}\frac{(g_e\mu_B\delta B_{\mathrm{dec},y'})^2}{D_{\mathrm{gs}} - g_e\mu_B B_z},\\
\delta E_{-1} ={}& -g_e\mu_B\delta B_{\mathrm{dec},z} + \frac{d_\perp^2\left(\delta\Pi^2_{\mathrm{dec},x'} + \delta\Pi^2_{\mathrm{dec},y'}\right)}{2g_e\mu_B B_z}\\
&+ \frac{1}{\sqrt{2}}\frac{(g_e\mu_B\delta B_{\mathrm{dec},x'})^2}{D_{\mathrm{gs}} + g_e\mu_B B_z} + \frac{1}{\sqrt{2}}\frac{(g_e\mu_B\delta B_{\mathrm{dec},y'})^2}{D_{\mathrm{gs}} - g_e\mu_B B_z},\\
\delta E_0 ={}& -\frac{(g_e\mu_B\delta B_{\mathrm{dec},x'})^2}{D_{\mathrm{gs}} + g_e\mu_B B_z} - \frac{(g_e\mu_B\delta B_{\mathrm{dec},y'})^2}{D_{\mathrm{gs}} - g_e\mu_B B_z}.
\end{aligned} \tag{D14}$$

Considering the $|0\rangle \to |-1\rangle$ ODMR transition, the fluctuations of the resonance frequency are

$$\delta\nu_+ = \delta E_{+1} - \delta E_0 = g_e\mu_B\delta B_{\mathrm{dec},z} + \frac{d_\perp^2\left(\delta\Pi^2_{\mathrm{dec},x'} + \delta\Pi^2_{\mathrm{dec},y'}\right)}{2g_e\mu_B B_z}, \tag{D15}$$

where we neglegted the term proportional to $\delta B_{\mathrm{dec},x'}, \delta B_{\mathrm{dec},y'}$ because $D_{gs} \gg g_e\mu_B\delta B_{\mathrm{dec},x'}$, $g_e\mu_B\delta B_{\mathrm{dec},y'}$. In this scenario, the effect of fluctuations of the axial magnetic field δB_z is at first order, instead the effects of the fluctuating total electric fields $\delta\Pi_x$, $\delta\Pi_y$ are at the second order. This is due to the fact that, in this scenario, $\langle S_z\rangle = \pm 1$ for $|S_z = \pm 1\rangle$.

Following the same line of thought of the previous subsection, it can be shown that the FID decay is characterized by a coherence time

$$T^*_{2,\text{strong field}} = \frac{1}{\sqrt{2}\pi}\frac{1}{\sqrt{(g_e\mu_B)^2\sigma^2_{B_{\mathrm{dec},z}} + \frac{d_\perp^4(\sigma^4_{\Pi_{\mathrm{dec},x}} + \sigma^4_{\Pi_{\mathrm{dec},y}})}{(2g_e\mu_B B_z)^2}}}. \tag{D16}$$

In this scenario, the more effective source of decoherence is related to $B_{\mathrm{dec},z}$, i.e., the coupling with the different spin baths and the temporal fluctuations of the external magnetic field.

3. Limit case: Intermediate axial fields

If we consider the condition

$$\mathcal{B}_\parallel \sim \sqrt{\mathcal{E}^2 + \frac{\mathcal{B}_\perp^2}{D_{\mathrm{gs}}}} \tag{D17}$$

the eigenstates are partially dressed states $|0\rangle, |-\rangle_{\theta,\mathcal{B}_z}, |+\rangle_{\theta,\mathcal{B}_\parallel}$ [see (Eq. (8)]. The fluctuations $\delta B_{\mathrm{dec}_i}$ and $\delta\Pi_{\mathrm{dec},i}$ induce the fluctuations in the eigenergies (until the first order):

$$\begin{aligned}
\delta E_{+,\theta,\mathcal{B}_\parallel} &= g_e\mu_B\delta B_{\mathrm{dec},z}\cos(\gamma) + d_\perp\delta\Pi_{\mathrm{dec},x'}\sin(\gamma),\\
\delta E_{-,\theta,\mathcal{B}_\parallel} &= -g_e\mu_B\delta B_{\mathrm{dec},z}\cos(\gamma) - d_\perp\delta\Pi_{\mathrm{dec},x'}\sin(\gamma),\\
\delta E_0 &= -\frac{(g_e\mu_B\delta B_{\mathrm{dec},x'})^2}{D_{gs} + g_e\mu_B B_z} - \frac{(g_e\mu_B\delta B_{\mathrm{dec},y'})^2}{D_{gs} - g_e\mu_B B_z},
\end{aligned} \tag{D18}$$

where $\tan(\gamma) = \frac{E_{\mathrm{gap}}/2}{g_e\mu_B B_\parallel}$ [see Eqs. (B7)].

We underline that in Eq. (D18), the relative weight of $\delta B_{\mathrm{dec},z}$ and $\delta\Pi_{\mathrm{dec},y'}$ is set by the expectation value of $\langle S_z\rangle$ and $\langle S_x^2 - S_y^2\rangle$, $\langle S_xS_y + S_yS_x\rangle$ on the eigenstates, e.g., $\langle +|S_z|+\rangle_{B_z} = \cos(\gamma)$.

Considering the $|0\rangle \to |+\rangle_{\theta,B_\parallel}$ ODMR transition, the fluctuation of the resonance frequency is

$$\begin{aligned}
\delta\nu_+ &= \delta E_{+,\theta,\mathcal{B}_\parallel} - \delta E_0\\
&= +g_e\mu_B\delta B_{\mathrm{dec},z}\cos(\gamma) + d_\perp\delta\Pi_{\mathrm{dec},y'}\sin(\gamma).
\end{aligned} \tag{D19}$$

Following the same line of thought of the previous subsections, it can be shown that the FID decay is characterized by a coherence time

$$T^*_{2,\text{part-dressed}} = \frac{1}{\sqrt{2}\pi}\frac{1}{\sqrt{(g_e\mu_B)^2\sigma^2_{B_{\mathrm{dec},z}}\cos(\gamma) + d_\perp^2\sigma^2_{\Pi_{\mathrm{dec},y'}}\sin(\gamma)}}. \tag{D20}$$

So, in this scenario, decoherence is due both to $B_{\text{dec},z'}$ and to $\Pi_{\text{dec},y'}$. The relative weights of the two different contributions depend on γ.

Summarizing for all three scenarios:

(i) The FID decay is a stretched exponential with $p = 2$.

(ii) The FID decay is characterized by a coherence time T_2^*.

(iii) The value of the static fields defines the effectiveness of the different sources of decoherence.

APPENDIX E: DECOHERENCE FOR AN ENSEMBLE OF NV CENTERS

Let us consider now an ensemble of NV's. In general, we have to start from the expression of the FID decay for a single NV center in Eq. (D2) and average over the NV's ensemble. The FID decay depends on variance of the phase fluctuation $\langle\delta\phi^2\rangle$ and on the detuning Δ between the microwave excitation frequency ν_{MW} and the ODMR transition $\Delta = \nu_{\text{MW}} - \nu_{-,\theta,\mathcal{B}_\parallel}$. In principle, both $\langle\delta\phi^2\rangle$ and $\nu_{-,\theta,\mathcal{B}_\parallel}$, and consequentely Δ take different values for the different spins of the ensemble following distributions $P(\langle\delta\phi^2\rangle)$ and $f(\Delta)$. Let us consider two cases:

(i) Δ does not vary over the ensemble. In this case we neglect gradients in the static fields $\vec{B}$ and $\vec{\Pi}$.

(ii) Δ varies over the ensemble. In this case we consider gradients in the static fields $\vec{B}$ and $\vec{\Pi}$.

1. Δ does not vary over the ensemble

In this case we have $f(\Delta) = \delta(\Delta)$. The problem is to develop a suitable expression for $P(\langle\delta\phi^2\rangle)$. If we now consider the strong-axial-field scenario, and we neglect the effect due to fourth-order fluctuations, from Eqs. (D3) and (D15) we have that $\langle\delta\phi^2\rangle$ depends only on the variance of the fluctuating field $\sigma_{B\text{-dec},z}$:

$$\langle\delta\phi^2\rangle_{\text{strong-field}} = 4\pi^2 g_e^2 \mu_B^2 \sigma_{B_{\text{dec},z}}^2 \tau^2. \tag{E1}$$

If $\sigma_{B\text{-dec},z}$ is mainly related to dipolar coupling, it can be shown that it is distributed as [56]

$$P\left(\sigma_{B_{\text{dec},z}}\right) = \frac{\sigma_{B_{\text{dec},z\text{-ens}}}}{\sigma_{B_{\text{dec},z}}^2}\sqrt{\frac{2}{\pi}}e^{-\sigma_{B_{\text{dec},z\text{ens}}}^2/2\sigma_{B_{\text{dec},z}}^2}, \tag{E2}$$

where $\sigma_{B_{\text{dec},z\text{-ens}}}$ is related to the average coupling strength of the NV to the spin bath within the NV ensemble. For a detailed discussion of $P(\sigma_{B\text{-dec},z})$ see Ref. [57]. This distribution has a maximum at $\sigma_{B_{\text{dec},z}} = \frac{\sigma_{B_{\text{dec},z\text{-ens}}}}{\sqrt{2}}$ and very heavy tails for higher values of $\sigma_{B_{\text{dec},z}}$.

Considering the FID decay for a single NV center in the strong axial field case, $p_{\text{FID}}^{\text{strong-field}}(\tau)$, from Eqs. (D2) and (E1), we have

$$\begin{aligned} p_{\text{FID}}^{\text{strong-field}}(\tau) &= \frac{\left[1 - e^{-\langle\delta\phi^2\rangle/2}\cos 2\pi\Delta\tau\right]}{2} \\ &= \frac{\left[1 - e^{-2\pi^2 g_e^2\mu_B^2\sigma_{B_{\text{dec},z}}^2\tau^2}\cos 2\pi\Delta\tau\right]}{2}. \end{aligned} \tag{E3}$$

To calculate the FID decay of the ensemble, we have to average $p_{\text{FID}}^{\text{strong-field}}(\tau)$ on $P(\sigma_{B_{\text{dec},z}})$:

$$\begin{aligned} p_{\text{FID}}^{\text{ens-strong-field}}(\tau) &= \int_0^\infty p_{\text{FID}}\left(\tau, \sigma_{B_{\text{dec},z}}\right)P\left(\sigma_{B_{\text{dec},z}}\right)d\sigma_{B_{\text{dec},z}} \\ &= \int_0^\infty p_{\text{FID}}\left(\tau, \sigma_{B_{\text{dec},z}}\right)P\left(\sigma_{B_{\text{dec},z}}\right)d\sigma_{B_{\text{dec},z}} \\ &= \int_0^\infty \frac{\left[1 - e^{-2\pi^2 g_e^2\mu_B^2\sigma_{B_{\text{dec},z}}^2\tau^2}\cos(2\pi\Delta\tau)\right]}{2}\frac{\sigma_{B_{\text{dec,z-ens}}}}{\sigma_{B_{\text{dec},z}}^2}\sqrt{\frac{2}{\pi}}e^{-\sigma_{B_{\text{dec},z\text{-ens}}}^2/2\sigma_{B_{\text{dec},z}}^2}d\sigma_{B_{\text{dec},z}} \\ &= \frac{\left[1 - \cos(2\pi\Delta\tau)\int_0^\infty e^{-2\pi^2 g_e^2\mu_B^2\sigma_{B_{\text{dec},z}}^2\tau^2}\frac{\sigma_{B_{\text{dec},z\text{-ens}}}}{\sigma_{B_{\text{dec},z}}^2}\sqrt{\frac{2}{\pi}}e^{-\sigma_{B_{\text{dec},z\text{-ens}}}^2/2\sigma_{B_{\text{dec},z}}^2}d\sigma_{B_{\text{dec},z}}\right]}{2} \\ &= \frac{[1 - \cos(2\pi\Delta\tau)I]}{2}. \end{aligned} \tag{E4}$$

The integral I in the previous equation is

$$\begin{aligned} I &= \int_0^\infty e^{-2\pi^2 g_e^2\mu_B^2\sigma_{B_{\text{dec},z}}^2\tau^2}\frac{\sigma_{B_{\text{dec},z\text{-ens}}}}{\sigma_{B_{\text{dec},z}}^2}\sqrt{\frac{2}{\pi}}e^{-\sigma_{B_{\text{dec},z\text{-ens}}}^2/2\sigma_{B_{\text{dec},z}}^2}d\sigma_{B_{\text{dec},z}} \\ &= \int_0^\infty \sqrt{\frac{2}{\pi}}\frac{\sigma_{B_{\text{dec},z\text{-ens}}}}{\sigma_{B_{\text{dec},z}}^2}e^{(-2\pi^2 g_e^2\mu_B^2\sigma_{B_{\text{dec},z}}^2\tau^2 - \sigma_{B_{\text{dec},z\text{-ens}}}^2/2\sigma_{B_{\text{dec},z}}^2)}d\sigma_{B_{\text{dec},z}} \\ &= e^{-2\pi g_e\mu_B\sigma_{B_{\text{dec},z\text{-ens}}}\tau}. \end{aligned} \tag{E5}$$

The detailed derivation of the integral is given in the Supplemental Material [44] (see also Ref. [65] therein). From Eqs. (E4) and (E5), the FID decay of the ensemble results:

$$p_{\mathrm{FID}}^{\text{ens-strong-field}}(\tau)=\frac{[1-e^{-2\pi g_e\mu_B\sigma_{B_{\mathrm{dec},z\text{-ens}}}\tau}\cos(2\pi\Delta\tau)]}{2}=\frac{\left[1-e^{-\frac{\tau}{T^*_{2,\text{ens,strong-field}}}}\cos(2\pi\Delta\tau)\right]}{2} \tag{E6}$$

with

$$T^*_{2,\text{ens,strong-field}}=\frac{1}{2\pi g_e\mu_B\sigma_{B_{\mathrm{dec},z\text{-ens}}}}. \tag{E7}$$

From the previous equations, it is clear that the ensemble-averaged FID decay is a simple exponential, $p=1$.

If we now consider the dressed states scenario, and we neglect the effect due to fourth-order fluctuations, $\langle\delta\phi^2\rangle$ depends only on $\sigma_{\Pi_{\mathrm{dec},x'}}$.

If we consider $\sigma_{\Pi_{\mathrm{dec},x'}}$ as mainly related to temporal fluctuations, we can consider that it does not vary over the NV's ensemble, formally $P(\sigma_{\Pi_{\mathrm{dec},x'}})=\delta(\sigma_{\Pi_{\mathrm{dec},x'}}-\sigma_{\Pi_{\mathrm{dec},x'-ens}})$, involving a Dirac δ function.

Integrating $p_{\mathrm{FID}}(\tau)$ over the distribution $P(\sigma_{\Pi_{\mathrm{dec},y'}})$, the ensemble-averaged decay results:

$$p_{\mathrm{FID}}^{\text{ens-dressed}}(\tau)=\frac{\left[1-\int e^{-d_\perp^2\sigma^2_{\Pi_{\mathrm{dec},x'}}\tau^2}\cos(2\pi\Delta\tau)\delta\left(\sigma_{\Pi_{\mathrm{dec},x'}}-\sigma_{\Pi_{\mathrm{dec},x'\text{-ens}}}\right)d\sigma_{\Pi_{dec,x'}}\right]}{2}=\frac{\left[1-e^{-(\frac{\tau}{T^*_{2,\text{ens-dressed}}})^2}\cos(2\pi\Delta\tau)\right]}{2}. \tag{E8}$$

The ensemble-averaged decay is a stretched exponential ($p=2$) with

$$T^*_{2,\text{ens-dressed}}=\frac{1}{d_\perp\sigma_{\Pi_{\mathrm{dec},x'\text{-ens}}}}. \tag{E9}$$

If we now consider the partially dressed states scenario, $\langle\delta\phi^2\rangle$ depends only both on $\sigma_{\Pi\text{-dec},y'}$ and $\sigma_{B_{\mathrm{dec},z}}$. If we use $P(\sigma_{B_{\mathrm{dec},z}})$ and $P(\sigma_{\Pi_{\mathrm{dec},x'}})$ defined before, the ensemble-averaged decay takes the form

$$\begin{aligned}p_{\mathrm{FID}}^{\text{ens-part-dressed}}(\tau)&=\frac{\left[1-\int e^{[-\cos(\gamma)g_e^2\mu_B^2\sigma_{B_{\mathrm{dec},z}}-\sin(\gamma)d_\perp^2\sigma^2_{\Pi_{\mathrm{dec},y}}]\tau^2}\cos(2\pi\Delta\tau)P\left(\sigma_{B_{\mathrm{dec},z}}\right)P\left(\sigma_{\Pi_{\mathrm{dec},y'}}\right)d\sigma_{\Pi_{\mathrm{dec},y'}}d\sigma_{B_{\mathrm{dec},z}}\right]}{2}\\&=\frac{\left[1-\cos(2\pi\Delta\tau)\int e^{-\cos(\gamma)g_e^2\mu_B^2\sigma^2_{B_{dec,z}}\tau^2}P\left(\sigma_{B_{\mathrm{dec},z}}\right)d\sigma_{B_{dec,z}}\int e^{-\sin(\gamma)d_\perp^2\sigma^2_{\Pi_{\mathrm{dec},y}}\tau^2}P\left(\sigma_{\Pi_{\mathrm{dec},y'}}\right)d\sigma_{\Pi_{\mathrm{dec},y'}}\right]}{2}\\&=\frac{\left[1-e^{-\cos(\gamma)\frac{\tau}{T^*_{2,\text{ens,strong-field}}}}e^{-\sin(\gamma)(\frac{\tau}{T^*_{2,\text{ens-dressed}}})^2}\cos(2\pi\Delta\tau)\right]}{2}.\end{aligned} \tag{E10}$$

The ensemble-averaged decay is a product of a simple exponential with a stretched exponential. The relative weight of the two exponentials is set by γ with $\tan(\gamma)=\frac{E_{\mathrm{gap}}/2}{g\mu_B B_z}$. The details of calculations of Eq. (E10) can be found in Supplemental Material [44].

Summarizing, in the absence of field gradients, at $B_z=0$, the decay will be close to a stretched exponential with $p=2$; for high axial field B_z, the decay will be close to a simple exponential; for intermediate values of B_z the decay is a product of a simple exponential and a stretched exponential.

2. **Δ varies over the ensemble**

Let us start neglecting the decoherence for the single NV. In this case, $\langle\delta\phi^2\rangle=0$ for every NV center in the ensemble, i.e., $P(\langle\delta\phi^2\rangle)=\delta(\langle\delta\phi^2\rangle)$. Instead, we consider that the static field $\vec{B}$ and $\vec{\Pi}'_y$ varies over the ensemble, following distributions $f_B(B)$ and $f_\Pi(\Pi)$. This will induce a distribution on the resonant frequencies $\nu_{-,\theta,\mathcal{B}_\parallel}$, which is computed from the differences in the eigenergies [see Eq. (B7)] and, consequently, a distribution $f_\Delta(\Delta)$ in the detunings $\Delta=\nu_{\mathrm{MW}}-\nu_{-,\theta,\mathcal{B}_\parallel}$

The ensemble-averaged decay takes the form

$$\begin{aligned}p_{\mathrm{FID}}^{\text{ens-gradient-sf}}(\tau)&=1-\int\cos(2\pi\Delta\tau)f_\Delta(\Delta)d\Delta\\&=1-1/2\left(\int e^{2\pi i\Delta\tau}f_\Delta(\Delta)d\Delta+\int e^{-2\pi i\Delta\tau}f_\Delta(\Delta)d\Delta\right)\\&=1-1/2[\tilde{f_\Delta}(\tau)+\tilde{f_\Delta}(\tau)^*].\end{aligned} \tag{E11}$$

The ensemble-averaged decay involves the Fourier transform $\tilde{f_\Delta}(\tau)$ of the distribution of detuning $f_\Delta(\Delta)$.

If we now consider that the single NV is subject to dechoerence in the strong-axial-field scenario, from Eq. (E6), we have

$$p_{\rm FID}^{\text{ens-gradient-dressed}}(\tau) = \frac{\left[1-\int e^{-\frac{\tau}{T^*_{2,\text{ens,strong-field}}}}\cos(2\pi\Delta\tau)f_\Delta(\Delta)d\Delta\right]}{2} = \frac{\left[1-e^{-\frac{\tau}{T^*_{2,\text{ens,strong-field}}}}[\tilde{f_\Delta}(\tau)+\tilde{f_\Delta}(\tau)^*]\right]}{4}, \tag{E12}$$

where we use the fact that $T^*_{2,\text{ens,strong-field}} \neq T^*_{2,\text{ens,strong-field}}(\Delta)$. The ensemble-averaged decay involves the product of the pure exponential with $p = 1$ and the Fourier transform $\tilde{f_\Delta}(\tau)$ of the distribution of detuning $f_\Delta(\Delta)$.

If we now consider the dressed-state scenario, from Eq. (E8), we have

$$p_{\rm FID}^{\text{ens-gradient-dressed}}(\tau) = \frac{\left[1-\int e^{-(\frac{\tau}{T^*_{2,\text{ens,dressed}}})^2}\cos(2\pi\Delta\tau)f_\Delta(\Delta)d\Delta\right]}{2} = \frac{\left[1-e^{-(\frac{\tau}{T^*_{2,\text{ens,dressed}}})^2}[\tilde{f_\Delta}(\tau)+\tilde{f_\Delta}(\tau)^*]\right]}{4}, \tag{E13}$$

where we use the fact that $T^*_{2,\text{ens,dressed}} \neq T^*_{2,\text{ens,dressed}}(\Delta)$. The ensemble-averaged decay involves the product of the stretched exponential with p=2 and the Fourier transform $\tilde{f_\Delta}(\tau)$ of the distribution of detuning $f_\Delta(\Delta)$.

If we now consider the partially dressed-states scenario, from Eq. (E10), we have

$$p_{\rm FID}^{\text{ens}-\text{gradient}-\text{part}-\text{dressed}}(\tau) = \frac{\left[1-\int e^{-\cos(\gamma)\frac{\tau}{T^*_{2,\text{ens,strong-field}}}}e^{-\sin(\gamma)(\frac{\tau}{T^*_{2,\text{ens,dressed}}})^2}\cos(2\pi\Delta\tau)f_\Delta(\Delta)d\Delta\right]}{2} = \frac{\left[1-e^{-\cos(\gamma)\frac{\tau}{T^*_{2,\text{ens,strong-field}}}}e^{-\sin(\gamma)(\frac{\tau}{T^*_{2,\text{ens,dressed}}})^2}[\tilde{f_\Delta}(\tau)+\tilde{f_\Delta}(\tau)^*]\right]}{4}. \tag{E14}$$

The ensemble-averaged decay involves the product of the simple exponential, the stretched exponential with $p = 2$, and the Fourier transform $\tilde{f_\Delta}(\tau)$ of the distribution of detuning $f_\Delta(\Delta)$.

In summary, gradients in the static field change the time dependence of the decay. In particular, for a strong-axial-field scenario, it is no longer a simple exponential, and for a dressed-state scenario, it is no longer a stretched exponential with $p = 2$.

APPENDIX F: FREE INDUCTION DECAY MEASUREMENTS FOR STRONG-AXIAL-FIELD STATES

In Fig. 5, FID measurements recorded for the NV$_2$ family are reported (see Fig. 6). The $B_\parallel$ component can be calculated from the full range CW-ODMR spectrum in Fig. 6 yielding $B_\parallel \approx 3\ mT$.

The shorter T_2^* indicates the high-field character of the state (the complete list of T_2^* values can be found in Table I in the main text). The FID data were recorded by tuning the MW frequency in resonance with the central hyperfine peak, therefore, only a single detuning ($\nu = 2.16$ MHz) is visible in the graph. As described in the previous section,

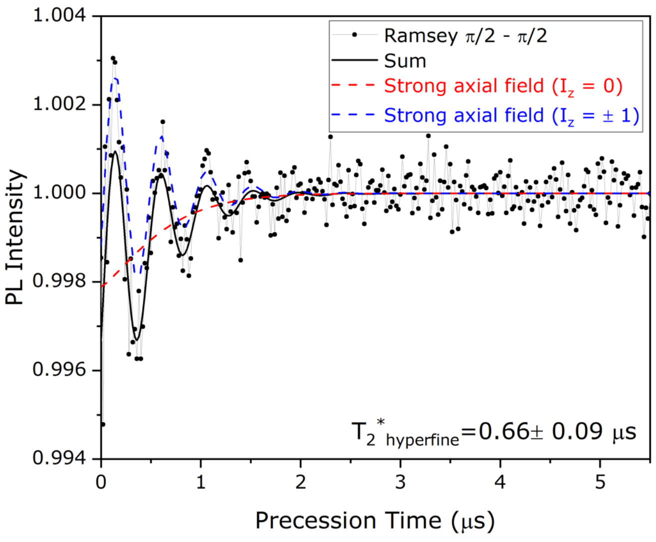

FIG. 5. FID relaxation for a microwave on resonance with the central peak of a hyperfine family at high fields.

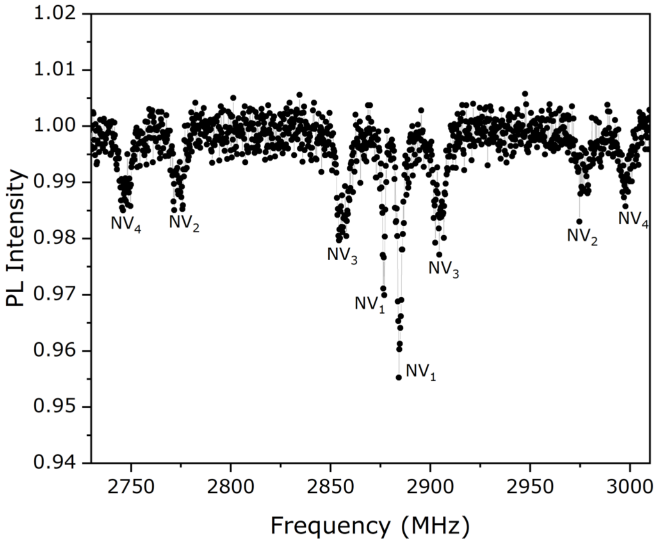

FIG. 6. CW-ODMR spectrum with identification of the crystallographic orientation.

strong-axial-field states couple with the spin bath and fluctuations of external magnetic fields, leading to shorter coherence times with respect to dressed states, where the largest sources of decoherence are electric fields and strain fluctuations.

[1] C. L. Degen, F. Reinhard, and P. Cappellaro, Quantum sensing, Rev. Mod. Phys. **89**, 035002 (2017).

[2] G. Petrini, E. Moreva, E. Bernardi, P. Traina, G. Tomagra, V. Carabelli, I. P. Degiovanni, and M. Genovese, Is a quantum biosensing revolution approaching? Perspectives in nv-assisted current and thermal biosensing in living cells, Adv. Quantum Technol. **3**, 2000066 (2020).

[3] E. Oh, M. D. Gregoire, A. T. Black, K. J. Hughes, P. D. Kunz, M. Larsen, J. Lautier-Gaud, J. Lee, P. D. D. Schwindt, S. L. Mouradian, F. A. Narducci, and C. A. Sackett, Perspective on quantum sensors from basic research to commercial applications, AIAA J. **62**, 4029 (2024).

[4] M. Genovese, Experimental quantum enhanced optical interferometry, AVS Quantum Sci. **3**, 044702 (2021).

[5] A. Karsa, A. Fletcher, G. Spedalieri, and S. Pirandola, Quantum illumination and quantum radar: A brief overview, Rep. Prog. Phys. **87**, 094001 (2024).

[6] R. G. Torromé and S. Barzanjeh, Advances in quantum radar and quantum lidar, Prog. Quantum Electron. **93**, 100497 (2024).

[7] G. Brida, M. Genovese, A. Meda, and I. R. Berchera, Experimental quantum imaging exploiting multimode spatial correlation of twin beams, Phys. Rev. A **83**, 033811 (2011).

[8] Y. Israel, S. Rosen, and Y. Silberberg, Supersensitive polarization microscopy using noon states of light, Phys. Rev. Lett. **112**, 103604 (2014).

[9] J. Aasi, J. Abadie, B. Abbott *et al.*, Enhanced sensitivity of the ligo gravitational wave detector by using squeezed states of light, Nat. Photonics **7**, 613 (2013).

[10] B. Stray, A. Lamb, A. Kaushik, J. Vovrosh, A. Rodgers, F. Winch, J. Hayati, D. Boddice, A. Stabrawa, A. Niggebaum, M. Langlois, Y.-H. Lien, S. Lellouch, S. Roshanmanesh, K. Ridley, G. de Villiers, G. Brown, T. Cross, G. Tuckwell, A. Faramarzi, and M. Holynski, Quantum sensing for gravity cartography, Nature (London) **602**, 590 (2022).

[11] S. Magaletti, L. Mayer, J.-F. Roch, and T. Debuisschert, A quantum radio frequency signal analyzer based on nitrogen vacancy centers in diamond, Commun. Eng. **1**, 19 (2022).

[12] S. Hernández-Gómez, T. Isogawa, A. Belenchia, A. Levy, N. Fabbri, S. Gherardini, and P. Cappellaro, Interferometry of quantum correlation functions to access quasiprobability distribution of work, npj Quantum Inf. **10**, 115 (2024).

[13] M. W. Doherty, F. Dolde, H. Fedder, F. Jelezko, J. Wrachtrup, N. B. Manson, and L. C. L. Hollenberg, Theory of the ground-state spin of the nv- center in diamond, Phys. Rev. B **85**, 205203 (2012).

[14] M. W. Doherty, N. B. Manson, P. Delaney, F. Jelezko, J. Wrachtrup, and L. C. L. Hollenberg, The nitrogen-vacancy in diamond, Phys. Rep. **528**, 1 (2013).

[15] L. Rondin, J.-P. Tetienne, T. Hingant, J.-F. Roch, P. Maletinsky, and V. Jacques, Magnetometry with nitrogen-vacancy defects in diamond, Rep. Prog. Phys. **77**, 056503 (2014).

[16] B. K. Ofori-Okai, S. Pezzagna, K. Chang, M. Loretz, R. Schirhagl, Y. Tao, B. A. Moores, K. Groot-Berning, J. Meijer, and C. L. Degen, Spin properties of very shallow nitrogen vacancy defects in diamond, Phys. Rev. B, **86**, 081406(R) (2012).

[17] D. M. Toyli, C. F. de Las Casas, D. J. Christle, V. V. Dobrovitski, and D. D. Awschalom, Fluorescence thermometry enhanced by the quantum coherence of single spins in diamond, Proc. Natl. Acad. Sci. USA **110**, 8417 (2013).

[18] P. Neumann, I. Jakobi, F. Dolde, C. Burk, R. Reuter, G. Waldherr, J. Honert, T. Wolf, A. Brunner, J. H. Shim *et al.*, High-precision nanoscale temperature sensing using single defects in diamond, Nano Lett. **13**, 2738 (2013).

[19] K. Fang, V. M. Acosta, C. Santori, Z. Huang, K. M. Itoh, H. Watanabe, S. Shikata, and R. G. Beausoleil, High-sensitivity magnetometry based on quantum beats in diamond nitrogen-vacancy centers, Phys. Rev. Lett. **110**, 130802 (2013).

[20] L. M. Pham, N. Bar-Gill, C. Belthangady, D. Le Sage, P. Cappellaro, M. D. Lukin, A. Yacoby, and R. L. Walsworth, Enhanced solid-state multispin metrology using dynamical decoupling, Phys. Rev. B **86**, 045214 (2012).

[21] P. Kehayias, M. Mrózek, V. M. Acosta, A. Jarmola, D. S. Rudnicki, R. Folman, W. Gawlik, and D. Budker, Microwave saturation spectroscopy of nitrogen-vacancy ensembles in diamond, Phys. Rev. B **89**, 245202 (2014).

[22] J. F. Barry, J. M. Schloss, E. Bauch, M. J. Turner, C. A. Hart, L. M. Pham, and R. L. Walsworth, Sensitivity optimization for nv-diamond magnetometry, Rev. Mod. Phys. **92**, 015004 (2020).

[23] G. Kucsko, P. C. Maurer, N. Y. Yao, M. Kubo, H. J. Noh, P. K. Lo, H. Park, and M. D. Lukin, Nanometre-scale thermometry in a living cell, Nature (London) **500**, 54 (2013).

[24] G. Petrini, G. Tomagra, E. Bernardi, E. Moreva, P. Traina, A. Marcantoni, F. Picollo, K. Kvaková, P. Cígler, I. P. Degiovanni *et al.*, Nanodiamond–quantum sensors reveal temperature variation associated to hippocampal neurons firing, Adv. Sci. **9**, 2202014 (2022).

[25] M. Fujiwara, S. Sun, A. Dohms, Y. Nishimura, K. Suto, Y. Takezawa, K. Oshimi, L. Zhao, N. Sadzak, Y. Umehara *et al.*, Real-time nanodiamond thermometry probing in vivo thermogenic responses, Sci. Adv. **6**, eaba9636 (2020).

[26] I. Lovchinsky, A. O. Sushkov, E. Urbach, N. P. de Leon, S. Choi, K. De Greve, R. Evans, R. Gertner, E. Bersin, C. Müller *et al.*, Nuclear magnetic resonance detection and spectroscopy of single proteins using quantum logic, Science **351**, 836 (2016).

[27] D. R. Glenn, D. B. Bucher, J. Lee, M. D. Lukin, H. Park, and R. L. Walsworth, High-resolution magnetic resonance spectroscopy using a solid-state spin sensor, Nature (London) **555**, 351 (2018).

[28] L. Thiel, D. Rohner, M. Ganzhorn, P. Appel, E. Neu, B. Müller, R. Kleiner, D. Koelle, and P. Maletinsky, Quantitative nanoscale vortex imaging using a cryogenic quantum magnetometer, Nat. Nanotechnol. **11**, 677 (2016).

[29] M. H. Abobeih, Y. Wang, J. Randall, S. J. H. Loenen, C. E. Bradley, M. Markham, D. J. Twitchen, B. M. Terhal, and T. H. Taminiau, Fault-tolerant operation of a logical qubit in a diamond quantum processor, Nature (London) **606**, 884 (2022).

[30] C. E. Bradley, J. Randall, M. H. Abobeih, R. C. Berrevoets, M. J. Degen, M. A. Bakker, M. Markham, D. J. Twitchen, and T. H. Taminiau, A ten-qubit solid-state spin register with quantum memory up to one minute, Phys. Rev. X **9**, 031045 (2019).

[31] G. L. Van de Stolpe, D. P. Kwiatkowski, C. E. Bradley, J. Randall, M. H. Abobeih, S. A. Breitweiser, L. C. Bassett, M. Markham, D. J. Twitchen, and T. H. Taminiau, Mapping a 50-spin-qubit network through correlated sensing, Nat. Commun. **15**, 2006 (2024).

[32] E. Moreva, E. Bernardi, P. Traina, A. Sosso, S. D. Tchernij, J. Forneris, F. Picollo, G. Brida, Ž. Pastuović, I. P. Degiovanni *et al.*, Practical applications of quantum sensing: A simple method to enhance the sensitivity of nitrogen-vacancy-based temperature sensors, Phys. Rev. Appl. **13**, 054057 (2020).

[33] E. H. Chen, H. A. Clevenson, K. A. Johnson, L. M. Pham, D. R. Englund, P. R. Hemmer, and D. A. Braje, High-sensitivity spin-based electrometry with an ensemble of nitrogen-vacancy centers in diamond, Phys. Rev. A **95**, 053417 (2017).

[34] C. S. Shin, C. E. Avalos, M. C. Butler, H.-J. Wang, S. J. Seltzer, R.-B. Liu, A. Pines, and V. S. Bajaj, Suppression of electron spin decoherence of the diamond nv center by a transverse magnetic field, Phys. Rev. B **88**, 161412 (2013).

[35] P. Jamonneau, M. Lesik, J. P. Tetienne, I. Alvizu, L. Mayer, A. Dréau, S. Kosen, J.-F. Roch, S. Pezzagna, J. Meijer *et al.*, Competition between electric field and magnetic field noise in the decoherence of a single spin in diamond, Phys. Rev. B **93**, 024305 (2016).

[36] F. Dolde, H. Fedder, M. W. Doherty, T. Nöbauer, F. Rempp, G. Balasubramanian, T. Wolf, F. Reinhard, L. C. L. Hollenberg, F. Jelezko *et al.*, Electric-field sensing using single diamond spins, Nat. Phys. **7**, 459 (2011).

[37] K. R. K. Rao and D. Suter, Level anti-crossings of a nitrogen-vacancy center in diamond: Decoherence-free subspaces and 3d sensors of microwave magnetic fields, New J. Phys. **22**, 083035 (2020).

[38] H. Clevenson, E. H. Chen, F. Dolde, C. Teale, D. Englund, and D. Braje, Diamond-nitrogen-vacancy electronic and nuclear spin-state anticrossings under weak transverse magnetic fields, Phys. Rev. A **94**, 021401(R) (2016).

[39] P. Lamba, A. Rana, S. Halder, S. Dhomkar, D. Suter, and R. K. Kamineni, Vector detection of ac magnetic fields by nitrogen vacancy centers of single orientation in diamond, Phys. Rev. B **109**, 195424 (2024).

[40] E. R. MacQuarrie, T. A. Gosavi, S. A. Bhave, and G. D. Fuchs, Continuous dynamical decoupling of a single diamond nitrogen-vacancy center spin with a mechanical resonator, Phys. Rev. B **92**, 224419 (2015).

[41] Z. Qiu, A. Hamo, U. Vool, T. X. Zhou, and A. Yacoby, Nanoscale electric field imaging with an ambient scanning quantum sensor microscope, npj Quantum Inf. **8**, 107 (2022).

[42] N. Wang, C.-F. Liu, J.-W. Fan, X. Feng, W.-H. Leong, A. Finkler, A. Denisenko, J. Wrachtrup, Q. Li, and R.-B. Liu, Zero-field magnetometry using hyperfine-biased nitrogen-vacancy centers near diamond surfaces, Phys. Rev. Res. **4**, 013098 (2022).

[43] N. Lambert, E. Giguère, P. Menczel, B. Li, P. Hopf, G. Suárez, M. Gali, J. Lishman, R. Gadhvi, R. Agarwal, A. Galicia, N. Shammah, P. Nation, J. R. Johansson, S. Ahmed, S. Cross, A. Pitchford, and F. Nori, Qutip 5: The quantum toolbox in python.

[44] See Supplemental Material at http://link.aps.org/supplemental/10.1103/3mlm-jjqq for the description of the experimental setup; calculation of total electric field inside the diamond sample; the fitting functions of free induction decay measurements; detailed calculation of the computation of the eigenstates; detailed calculation of the derivation of the probability distribution for the ensemble.

[45] T. Mittiga, S. Hsieh, C. Zu, B. Kobrin, F. Machado, P. Bhattacharyya, N. Z. Rui, A. Jarmola, S. Choi, D. Budker, and N. Y. Yao, Imaging the local charge environment of nitrogen-vacancy centers in diamond, Phys. Rev. Lett. **121**, 246402 (2018).

[46] M. A. Nielsen and I. L. Chuang, *Quantum Computation and Quantum Information: 10th Anniversary Edition* (Cambridge University Press, Cambridge, 2010).

[47] The trace distance $D(\rho, \sigma)$ between two density matrices ρ and σ is $D(\rho, \sigma) = \frac{1}{2}\mathrm{Tr}|\rho - \sigma|$.

[48] To be precise, there is an anticrossing between the $I_z = +1$ and $I_z = -1$ components at $B_\parallel = 0$. This anticrossing is due to the orthogonal part of the hyperfine term. These states are very fragile. They are destroyed by an axial magnetic field of around 100 nT and the energy gap created by the anticrossing is very small, around 2 kHz.

[49] H. Babashah, H. Shirzad, E. Losero, V. Goblot, C. Galland, and M. Chipaux, Optically detected magnetic resonance with an open source platform, SciPost Phys. Core **6**, 065 (2023).

[50] J. M. Binder, A. Stark, N. Tomek, J. Scheuer, F. Frank, K. D. Jahnke, C. Müller, S. Schmitt, M. H. Metsch, T. Unden *et al.*, Qudi: A modular python suite for experiment control and data processing, SoftwareX **6**, 85 (2017).

[51] K. Sasaki, Y. Monnai, S. Saijo, R. Fujita, H. Watanabe, J. Ishi-Hayase, K. M. Itoh, and E. Abe, Broadband, large-area microwave antenna for optically detected magnetic resonance of nitrogen-vacancy centers in diamond, Rev. Sci. Instrum. **87**, 053904 (2016).

[52] A. Dréau, M. Lesik, L. Rondin, P. Spinicelli, O. Arcizet, J.-F. Roch, and V. Jacques, Avoiding power broadening in optically detected magnetic resonance of single nv defects for enhanced dc magnetic field sensitivity, Phys. Rev. B **84**, 195204 (2011).

[53] M. Born and E. Wolf, *Principles of Optics: Electromagnetic Theory of Propagation, Interference and Diffraction of Light* (Elsevier, Amsterdam, 2013).

[54] R. Giri, F. Gorrini, C. Dorigoni, C. E. Avalos, M. Cazzanelli, S. Tambalo, and A. Bifone, Coupled charge and spin dynamics in high-density ensembles of nitrogen-vacancy centers in diamond, Phys. Rev. B **98**, 045401 (2018).

[55] In the usual terminology T_2^* is the time constant that describes the loss of coherence considering field inhomogeneities, T_2 is the time constant that describes the loss of coherence due solely to intrinsic sources, and T_1 is the time constant related to the relaxation to thermal equilibrium.

[56] E. Bauch, S. Singh, J. Lee, C. A. Hart, J. M. Schloss, M. J. Turner, J. F. Barry, L. M. Pham, N. Bar-Gill, S. F. Yelin *et al.*, Decoherence of ensembles of nitrogen-vacancy centers in diamond, Phys. Rev. B **102**, 134210 (2020).

[57] V. V. Dobrovitski, A. E. Feiguin, D. D. Awschalom, and R. Hanson, Decoherence dynamics of a single spin versus spin ensemble, Phys. Rev. B **77**, 245212 (2008).

[58] E. Bauch, C. A. Hart, J. M. Schloss, M. J. Turner, J. F. Barry, P. Kehayias, S. Singh, and R. L. Walsworth, Ultralong dephasing

times in solid-state spin ensembles via quantum control, Phys. Rev. X **8**, 031025 (2018).

[59] The spectral width of $\frac{\pi}{2}$ pulse is approximately equal to the Rabi frequency of the MW.

[60] N. Arunkumar, K. S. Olsson, J. T. Oon, C. A. Hart, D. B. Bucher, D. R. Glenn, M. D. Lukin, H. Park, D. Ham, and R. L. Walsworth, Quantum logic enhanced sensing in solid-state spin ensembles, Phys. Rev. Lett. **131**, 100801 (2023).

[61] we are, again, neglecting the effect of the anticrossing.

[62] J. F. Barry, M. J. Turner, J. M. Schloss, D. R. Glenn, Y. Song, M. D. Lukin, H. Park, and R. L. Walsworth, Optical magnetic detection of single-neuron action potentials using quantum defects in diamond, Proc. Natl. Acad. Sci. USA **113**, 14133 (2016).

[63] R. Pellicer-Guridi, K. Custers, J. Solozabal-Aldalur, A. Brodolin, J. T. Francis, M. Varga, A. Mongelos, J. Casanova, M. M. Paulides, and G. Molina-Terriza, Versatile quadrature antenna for precise control of large electron spin ensembles in diamond, Adv. Quantum Technol. **8**, 2400142 (2025).

[64] W. H. Zurek, Decoherence, einselection, and the quantum origins of the classical, Rev. Mod. Phys. **75**, 715 (2003).

[65] I. S. Gradshteyn and I. M. Ryzhik, *Table of Integrals, Series, and Products* (Academic, New York, 2014).